A&A manuscript no.
(will be inserted by hand later)

Your thesaurus codes are:
06(02.01.2, 02.08.1, 02.09.1, 02.19.1, 03.13.4, 08.02.1)

ASTRONOMY
AND
ASTROPHYSICS
15.10.1996

Non-axisymmetric wind-accretion simulations

I. Velocity gradients of 3% and 20% over one accretion radius

M. Ruffert[⋆]

Max-Planck-Institut für Astrophysik, Postfach 1523, D - 85740 Garching, Germany

October 15, 1996

Abstract. We investigate the hydrodynamics of a variant of classical Bondi-Hoyle-Lyttleton accretion: a totally absorbing sphere moves at various Mach numbers (3 and 10) relative to a medium, which is taken to be an ideal gas having a velocity gradient (of 3% or 20% over one accretion radius) perpendicular to the relative motion. We examine the influence of the Mach number of the flow and the strength of the gradient upon the physical behaviour of the flow and the accretion rates of the angular momentum in particular. The hydrodynamics is modeled by the "Piecewise Parabolic Method" (PPM). The resolution in the vicinity of the accretor is increased by multiply nesting several grids around the sphere.

Similarly to the 3D models without gradients published previously, models exhibit non-stationary flow patterns, although the Mach cone remains fairly stable. The accretion rates of mass, linear and angular momenta do not fluctuate as strongly as published previously for 2D models, but similarly to the 2D models, transient disks form around the accretor that alternate their direction of rotation with time. The average specific angular momentum accreted is roughly between 7% and 70% of the total angular momentum available in the accretion cylinder and is always smaller than the value of a vortex with Kepler velocity around the surface of the accretor. The fluctuations of the mass accretion rate in the models with small gradients (2%) are similar to the values of the models without gradients, while the models with large gradients (20%) exhibit larger fluctuations. The mass accretion rate is maximal when the specific angular momentum is zero, while the specific entropy tends to be smaller when the disks are prograde.

Key words: Accretion, accretion disks – Hydrodynamics – Instabilities – Shock waves – Methods: numerical – Binaries: close

⋆ e-mail: `mruffert@mpa-garching.mpg.de`

1. Introduction

The simplicity of the classic Bondi-Hoyle-Lyttleton (BHL) accretion model makes its use attractive in order to roughly estimate accretion rates and drag forces in many different astrophysical contexts, ranging from wind-fed X-ray binaries (e.g. Anzer & Börner 1995), over supernovae (e.g. Chevalier 1996), and galaxies moving through intracluster gas in a cluster of galaxies (Balsara et al. (1994), to the black hole believed to be at the center of our Galaxy (Ruffert & Melia 1994; Mirabel et al. 1991). In the BHL scenario a totally absorbing sphere of mass M moves with velocity v_∞ relative to a surrounding homogeneous medium of density ρ_∞ and sound speed c_∞. It has been investigated numerically by many workers (e.g. Ruffert 1994 and 1995, and references therein). Usually, the accretion rates of various quantities, like mass, angular momentum, etc., including drag forces are of interest as well as the properties of the flow, (e.g. distribution of matter and velocity, stability, etc.). All results pertaining to total accretion rates are in qualitative agreement (to within factors of two, ignoring the instablitites of the flow) with the original calculations of Bondi, Hoyle and Lyttleton (e.g. Ruffert & Arnett 1994).

The BHL recipe for accretion in the axisymmetric case for pressureless matter is the following. A ring of material with radius b (which is identical to the impact parameter) far upstream from the accretor and thickness db will be focussed gravitationally to a point along the radial accretion line downstream of the accretor. At this point the linear momentum perpendicular to the radial direction is assumed to be cancelled. Then, if the remaining energy of the matter at this point is not sufficient for escape from the potential, this material is assumed to be accreted. The largest radius b from which matter is still accreted by this procedure turns out to be the so-called Hoyle-Lyttleton accretion radius (Hoyle & Lyttleton 1939, 1940a, 1940b, 1940c; Bondi & Hoyle 1944)

$$R_{\rm A} = \frac{2GM}{v_\infty^2} \quad , \tag{1}$$

where G is the gravitational constant. The mass accretion rate follows to be

$$\dot{M}_{\rm HL} = \pi R_{\rm A}^2 \rho_\infty v_\infty \quad . \tag{2}$$

I will refer to the volume upstream of the accretor from which matter is accreted as accretion cylinder.

However, if the assumption of homogeneity of the surrounding medium is dropped, e.g. by assuming some constant gradient in the density or the velocity distribution, the consequences on the accretion flow remain very unclear. Using the same conceptual procedures, one can calculate (Dodd & McCrea 1952; Illarionov & Sunyaev 1975; Shapiro & Lightman 1976; Wang 1981) how much angular momentum is present in the accretion cylinder for a non-axisymmetric flow which has a gradient in its density or velocity perpendicular to the mean velocity direction. Then, assuming that the angular momentum will be accreted together with the mass, it is only a small step to conclude that the amount of angular momentum accreted is equal to (or at least is a large fraction of) the angular momentum present in the accretion cylinder. Note, that if the velocity is a function of position, then by virtue of Eq. (1) also the accretion radius varies in space. Thus the cross section of the accretion cylinder (perpendicular to the axis) is not circular.

However, the reasoning of BHL calls for a cancelling of linear momentum perpendicular to the radial accretion line before matter is accreted. Together with this linear momentum also angular momentum is cancelled and so the matter accreted has zero angular momentum by construction! This point was first discussed by Davies & Pringle (1980), who were able to construct two-dimensional flows with small non-vanishing gradients for which the accreted angular momentum was exactly zero, by placing the accretion line appropriately. Thus, following these analytic investigations two opposing views are voiced about how much angular momentum can be accreted: either a large or a very small fraction of what is present in the accretion cylinder. Numerical simulations thus are called for to help solve the problem.

In this paper I would like to compare the accretion rates of several quantities (especially angular momentum) of numerically modeled accretion flows with gradients to the previous results of accretion without gradients (e.g. Ruffert 1994). One has to change some of the parameters of the flow (Mach number, size of the accretor) in order to get a good overview of which features are generic and which specific to that combination of parameters. Although several investigations of *two*-dimensional flows with velocity gradients exist (Anzer et al. 1987; Fryxell & Taam 1988; Taam & Fryxell 1989; Ho et al. 1989), *three*-dimensional simulations are scarse due to their inherently high computational load. Livio et al. (1986) first attempted a three-dimensional model including gradients, but due to their low numerical resolution the results were only tentative. Also in the models of Ishii et al. (1993) was the accretor only coarsly resolved, while the results of Boffin (1991) and Sawada et al. (1989) are only indicative, because due to the numerical procedure the flows remained stable (too few SPH particles in Boffin 1991 and local time stepping in Sawada et al. 1989 which is appropriate only for stationary flows). A simulation that was numerically better resolved was performed later by Ruffert & Anzer (1995), but since only one model was presented, the results cannot be taken as conclusive either. I intend to remedy these shortcomings in the present paper.

In Sect. 2 I give only a short summary of the numerical procedure used. Sections 4 to 6 present the results, which I analyze and interpret in Sect. 8. Section 9 summarizes the implications of this work.

2. Numerical Procedure and Initial Conditions

Since the numerical procedures and initial conditions are mostly identical to what has already been described and used in previous papers (e.g. Ruffert, 1996; Ruffert & Anzer, 1994) I will refrain from repeating every detail, but only give a brief summary.

2.1. Numerical Procedure

The distribution of matter is discretised on multiply nested equidistant Cartesian grids (e.g. Berger & Colella, 1989) with zone size δ and is evolved using the "Piecewise Parabolic Method" (PPM) of Colella & Woodward (1984). The equation of state is that of a perfect gas with a specific heat ratio of $\gamma = 5/3$ or $\gamma = 4/3$ (see Table 1). The model of the maximally accreting, vacuum sphere in a softened gravitational potential is summarized in Ruffert & Arnett (1994) and Ruffert & Anzer (1995).

A gravitating, totally absorbing "sphere" moves relative to a medium that far upstream has a distribution of density and velocity given by

$$\rho_\infty = \rho_0 \left(1 + \varepsilon_\rho \frac{y}{R_{\rm A}} \right) \quad , \tag{3}$$

$$v_{{\rm x}\infty} = v_0 \left(1 + \frac{1}{2} \tanh \left[2\varepsilon_{\rm v} \frac{y}{R_{\rm A}} \right] \right) , \ v_{{\rm y}\infty} = 0, \ v_{{\rm z}\infty} = 0 \ , \tag{4}$$

with the redefined accretion radius

$$R_{\rm A} = \frac{2GM}{v_0^2} \quad . \tag{5}$$

In this paper I only investigate models with gradients of the velocity distribution; the values of $\varepsilon_{\rm v}$ can be found in Table 1. Thus for all models I set $\varepsilon_\rho \equiv 0$. Additionally, if only a density gradient is introduced without varying some other thermodynamic variable (e.g. temperature, entropy, etc.) at the same rate, pressure will not be in equilibrium (cf. e.g. Ho et al. 1989), so an additional thermodynamic variable should be varied, which complicates matters.

Table 1. Parameters and some computed quantities for all models. $\mathcal{M}_\infty$ is the Mach number of the unperturbed flow, ε_v the parameter specifying the strength of the gradient, γ the ratio of specific heats, $R_\star$ the radius of the accretor, g the number of grid nesting depth levels, δ the size of one zone on the finest grid, ϵ the softening parameter (zones) for the potential of the accretor (see Ruffert, 1994), t_f the total time of the run (units: R_A/c_∞), $\overline{\dot M}$ the integral average of the mass accretion rate, S one standard deviation around the mean $\overline{\dot M}$ of the mass accretion rate fluctuations, $\widehat{\dot M}$ the maximum mass accretion rate, $\dot M_\mathrm{BH}$ is defined in Eq. (3) of Ruffert & Arnett (1994), l_x, l_y, l_z, are the averages of specific angular momentum components together with their respective standard deviations σ_x, σ_y, σ_z, s is the entropy (Eq. (4) in Ruffert & Arnett 1994), the number N of zones per grid dimension is 32, and the size of the largest grid is $L = 32R_\mathrm{A}$ (except for model RL for which it is $L = 128R_\mathrm{A}$).

Model	$\mathcal{M}_\infty$	ε_v	γ	$R_\star$ (R_A)	g	δ (R_A)	ϵ	t_f	$\overline{\dot M} \pm S$ ($\dot M_\mathrm{BH}$)	$\widehat{\dot M}$ ($\dot M_\mathrm{BH}$)	$l_\mathrm{x} \pm \sigma_\mathrm{x}$ ($1.5\,\varepsilon_\mathrm{v} R_\mathrm{A} v_0$)	$l_\mathrm{y} \pm \sigma_\mathrm{y}$ ($1.5\,\varepsilon_\mathrm{v} R_\mathrm{A} v_0$)	$l_\mathrm{z} \pm \sigma_\mathrm{z}$ ($1.5\,\varepsilon_\mathrm{v} R_\mathrm{A} v_0$)	s ($\mathcal{R}$)
IT	3	-0.03	5/3	0.02	10	1/512	8	4.82	0.72 ± 0.04	0.78	0.00 ± 0.01	0.00 ± 0.02	+0.20 ± 0.04	2.1
IS	3	-0.03	5/3	0.02	9	1/256	3	13.9	0.53 ± 0.09	0.80	0.00 ± 0.13	0.05 ± 0.17	+0.12 ± 0.24	2.2
IM	3	-0.03	5/3	0.10	7	1/64	4	26.6	0.79 ± 0.06	0.90	-0.01 ± 0.11	0.00 ± 0.13	+0.68 ± 0.33	2.2
IM*	3	-0.03	5/3	0.10	7	1/64	4	8.37	0.82 ± 0.08	0.91	+0.02 ± 0.06	-0.08 ± 0.14	+0.69 ± 0.45	2.2
JS	10	-0.03	5/3	0.02	9	1/256	3	2.93	0.45 ± 0.09	0.68	-0.04 ± 0.17	-0.08 ± 0.35	+0.18 ± 0.28	5.3
JM	10	-0.03	5/3	0.10	7	1/64	4	10.3	0.72 ± 0.05	0.79	+0.01 ± 0.06	-0.07 ± 0.33	+0.26 ± 0.35	5.2
KS	3	-0.20	5/3	0.02	9	1/256	3	6.89	0.54 ± 0.09	0.78	0.00 ± 0.02	-0.01 ± 0.03	+0.07 ± 0.02	1.8
KM	3	-0.20	5/3	0.10	7	1/64	4	20.3	0.95 ± 0.19	1.30	0.00 ± 0.02	0.00 ± 0.02	+0.26 ± 0.06	1.6
LS	10	-0.20	5/3	0.02	9	1/256	3	1.94	0.35 ± 0.08	0.53	+0.02 ± 0.03	+0.01 ± 0.05	+0.09 ± 0.03	5.2
LM	10	-0.20	5/3	0.10	7	1/64	4	8.54	0.72 ± 0.17	1.11	0.00 ± 0.04	0.00 ± 0.05	+0.25 ± 0.09	4.7
RL	0.6	-0.20	5/3	1.00	6	1/8	5	63.1	36.3 ± 0.14	36.4	0.00 ± 0.00	0.00 ± 0.00	-0.49 ± 0.04	0.18
ST	3	-0.03	4/3	0.02	10	1/512	8	4.60	1.01 ± 0.09	1.29	0.00 ± 0.05	+0.01 ± 0.07	+0.51 ± 0.23	4.4
SS	3	-0.03	4/3	0.02	9	1/256	3	9.24	1.01 ± 0.12	1.46	+0.02 ± 0.15	+0.03 ± 0.25	+0.36 ± 0.40	5.2

The function “tanh” is introduced in Eq. (4) to serve as a cutoff at large distances y for large gradients ε_v: In some models I imposed a gradient of $\varepsilon_\mathrm{v} = 0.2$ which at distances beyond $5R_\mathrm{A}$ would produce negative velocities if a linear distribution were used. In the limit of small $y \ll R_\mathrm{A}$, Eq. (4) transforms to a shape very similar to Eq. (3) with ρ replaced by v (as in Ruffert & Anzer 1995, Eq. (2)). The relative velocity v_0 is varied in different models: I perform simulations with Mach numbers $\mathcal{M}_\infty \equiv v_0/c_\infty$ of 3.0 and 10. In the reference frame of the accretor the surrounding matter flows in +x-direction. Our units are (1) the sound speed c_∞ as velocity unit; (2) the accretion radius (Eq. (5)) as unit of length, and (3) $\rho_\infty = \rho_0$ as density unit. Thus the unit of time is R_A/c_∞.

When using the density and velocity distributions (Eqs. (3) and (4)) to calculate the mass accretion rate, assuming that all mass within the accretion cylinder is accreted, one obtains to lowest order in ε_v

$$\dot M = \pi R_\mathrm{A}^2 \rho_0 v_0 \quad , \tag{6}$$

an equation very similar to Eq. (2). Further assuming that all angular momentum within the deformed accretion cylinder is accreted too, the specific angular momentum of the accreted matter follows to be (Ruffert & Anzer 1994; Shapiro & Lightman 1976; again to lowest order in ε_v)

$$j_z = \frac{1}{4}\left(6\varepsilon_\mathrm{v} - \varepsilon_\rho\right) v_0 R_\mathrm{A} \quad . \tag{7}$$

Note the different signs with which the two ε enter this equation. The density gradient ε_ρ acts in the “expected” direction: if the density is higher on the positive side of the y-axis, then the vortex formed around the accretor is in the counter-clockwise direction, i.e. the angular momentum is negative. Contrary to this, if the velocity is larger on the positive y-side, then the shortened accretion radius on this side reduces the cross-section for the higher specific angular momentum to such an extent that the rotational direction of the vortex is reversed: the angular momentum is positive.

The values obtained from the numerical simulations of the specific angular momentum should be compared to the values that follow from this Eq. (7) to conclude which of the above mentioned views — low or high specific angular momentum of the accreted material — is most probably correct. Ruffert & Anzer (1995) find that the numerical value is 0.72 times[1] the analytical estimate, which would indicate a large value for the accreted specific angular momentum. Although the simulations yield the values of all three components of the angular momentum, the interesting component is the one pointing in z-direction. Thus I will implicitely assume j_z when discussing properties like fluctuations, magnitudes, etc. that the simulations produce. From the symmetry of the boundary conditions the

[1] this value is the rms, while in Table 1 we list the averages

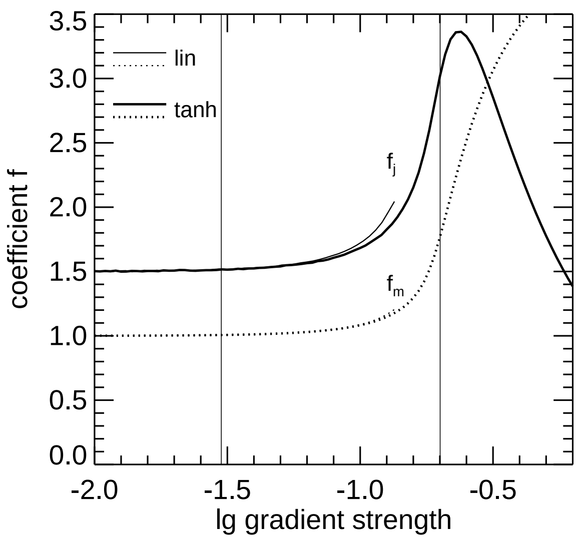

Fig. 1. The coefficient for the mass accretion rate f_{m} (dotted), defined by Eq. (8), and for the specific angular momentum f_{j} (solid), defined by Eq. (9), as a function of ε_{v}. The two thin curves that end at around -0.8 show the values of f for a simple linear relation between $v_{\mathrm{x}\infty}$ and ε_{v}, while the bold curves apply to a relation including the "tanh"-term as given in Eq. (4). The two vertical straight lines indicate the gradients that were used in the numerical models (cf. Table 1), $\varepsilon_{\mathrm{v}} = 0.03$ and $\varepsilon_{\mathrm{v}} = 0.2$.

average of the x and y components of the angular momentum should be zero, although their fluctuations can be quite large. Numerically I obtain the mass and angular momentum accretion rates as a function of time, $\dot{M}(t)$ and $\dot{J}(t)$. From these functions I calculate the instantaneous specific angular momentum $j(t) = \dot{J}(t)/\dot{M}(t)$ as function of time, which I will plot and from which I calculate the temporal mean l listed in Table 1.

One can numerically approximate the integrals (U. Anzer, personal communication) of the mass flux and angular momentum over the deformed cross section of the accretion cylinder, to obtain the coefficients f in the relations Eq. (6) and Eq. (7):

$$\dot{M} = f_{\mathrm{m}}(\varepsilon_{\mathrm{v}})\pi R_{\mathrm{A}}^2 \rho_0 v_0 \quad , \tag{8}$$

$$j_{\mathrm{z}} = f_{\mathrm{j}}(\varepsilon_{\mathrm{v}})\varepsilon_{\mathrm{v}} v_0 R_{\mathrm{A}} \quad . \tag{9}$$

Here, I will only consider the effect of a velocity gradient. The unitless functions f are a function of ε_{v} and the functional relation of $v_{\mathrm{x}\infty}[\varepsilon_{\mathrm{v}}]$, i.e. whether $v_{\mathrm{x}\infty}$ depends purely linearly on ε_{v} or as in Eq. (4) via the "tanh"-term. Figure 1 shows the values of the functions f for the mass and specific angular momentum and for both the linear and "tanh" case. In the linear case there is no solution for $\varepsilon_{\mathrm{v}} \gtrsim 0.15$ (U. Anzer, personal communication) so the curves end at that point. Since $f_{\mathrm{m}} \approx 1$ and is practically constant for $\varepsilon_{\mathrm{v}} \lesssim 0.1$, the Eq. (6) is a good approximation in this range. If the prescription is correct that everything in the accretion cylinder is accreted, we expect to see an increase of the mass accretion rate by a factor of roughly 1.8 in the models with a fairly large gradient of $\varepsilon_{\mathrm{v}} = 0.2$ (cf. Table 1). The same trends apply to the specific angular momentum: its coefficient f_{j} remains relatively constant $f_{\mathrm{j}} \approx 1.5$ in the range $\varepsilon_{\mathrm{v}} \lesssim 0.1$, and becomes a factor of 2 larger for $\varepsilon_{\mathrm{v}} \approx 0.2$. In the case including "tanh", the coefficent f_{j} decreases again for $\varepsilon_{\mathrm{v}} \gtrsim 0.25$ because the gradient is so steep that the "tanh"-cutoff acts at very short distances. So the short lever arm that enters into the angular momentum wins.

2.2. Models

The combination of parameters that I varied, together with some results are summarised in Table 1. The first letter in the model designation indicates the Mach number and the strength of the gradient: I, J, and S have $\varepsilon_{\mathrm{v}} = 0.03$, while K, L, and R have $\varepsilon_{\mathrm{v}} = 0.2$. The second letter specifies the size of the accretor: M (medium) and S (small) stand for accretor radii of $0.1\,R_{\mathrm{A}}$, and $0.02\,R_{\mathrm{A}}$, respectively. I basically simulated models with all possible combinations of two relative wind flow speeds (Mach numbers of 3 and 10), two gradient strengths (3% and 20%) and two different accretor sizes (0.02 and 0.1 accretion radii), all with an adiabtic index of 5/3. The exeptional models are ST and SS — in which I used an adiabatic index of 4/3 — and model RL which has a very large accretor radius and a very slow relative flow velocity. The grids are nested to a depth g such that the radius of the accretor $R_\star$ spans several zones on the finest grid and the softening parameter ϵ is then chosen to be a few zones less than the number of zones that the accretor spans. Model IT and ST are physically identical to models IS and SS, respectively. However, models IT and ST are numerically better resolved, because they are nested one grid level finer. Model IM is identical to the model presented in Ruffert & Anzer (1995), i.e. the velocity gradient is chosen as specified in Eq. (2) of Ruffert & Anzer (1995) without the "tanh"-term of Eq. (4). This term is included in model IM*, however, since the results were nearly indistinguishable between models IM and IM*, model IM* was evolved for only roughly one third of the time of model IM.

As far as computer resources permitted, I aimed at evolving the models for at least as long as it takes the flow to move from the boundary to the position of the accretor which is at the center (crossing time scale). This time is given by $L/2\mathcal{M}_\infty$ and ranges from about 1 to about 10 time units. The actual time t_{f} that the model is run can be found in Table 1.

The velocity distribution following the "tanh"-prescription of Eq. (4) has an inflection point and thus is Kelvin-Helmholz unstable with an amplification time constant of roughly $\tau \approx (5R_{\mathrm{A}})/(\varepsilon_{\mathrm{v}}\mathcal{M}c_\infty)$ (Drazin & Reid 1981). During the time it takes matter to move from

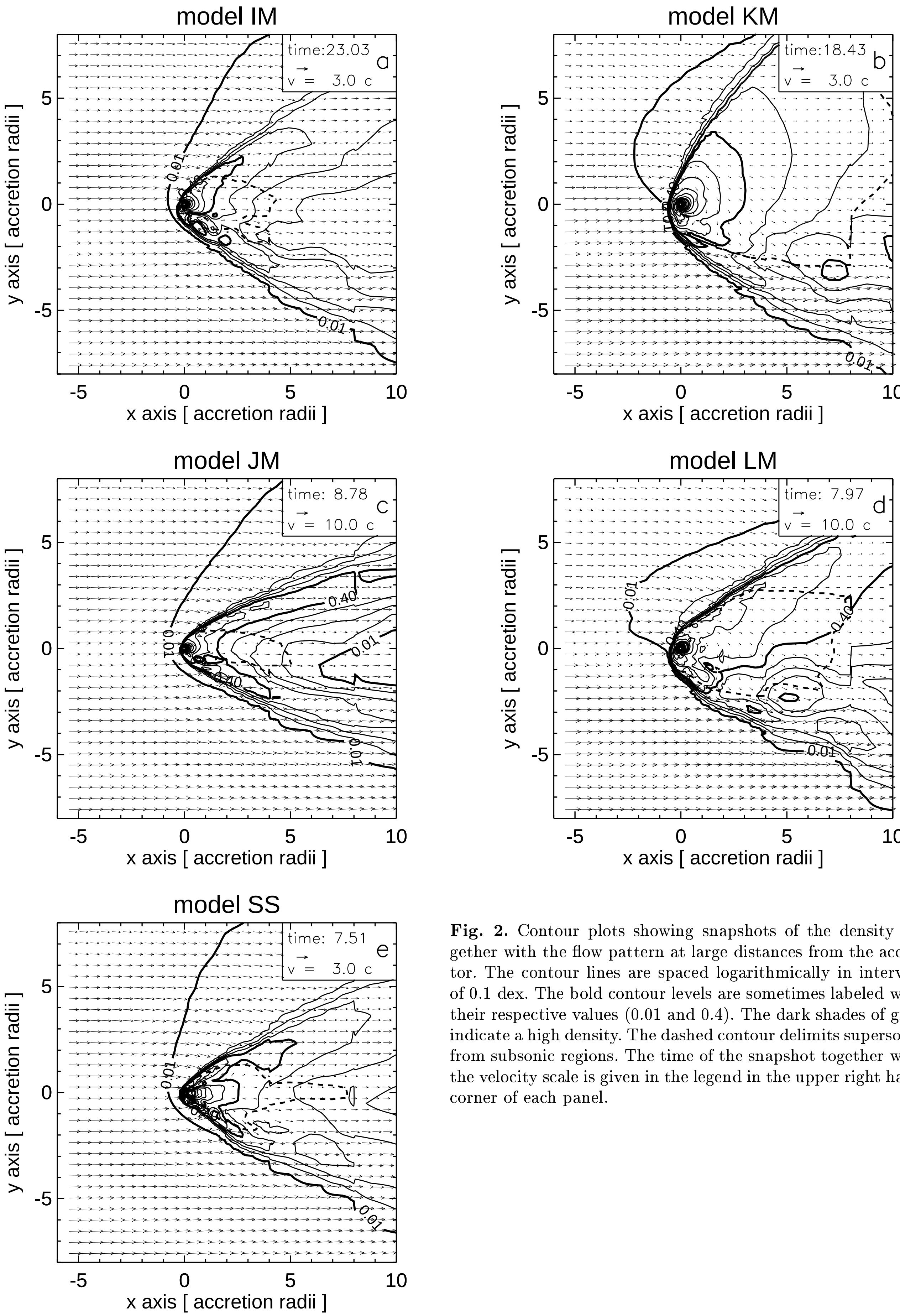

Fig. 2. Contour plots showing snapshots of the density together with the flow pattern at large distances from the accretor. The contour lines are spaced logarithmically in intervals of 0.1 dex. The bold contour levels are sometimes labeled with their respective values (0.01 and 0.4). The dark shades of gray indicate a high density. The dashed contour delimits supersonic from subsonic regions. The time of the snapshot together with the velocity scale is given in the legend in the upper right hand corner of each panel.

the boundary to the accretor, $t \approx (16R_{\rm A})/(\mathcal{M}c_\infty)$, random perturbations can grow by about $t/\tau \approx 3\varepsilon_{\rm v}$ which is smaller than unity even for the large gradients ($\varepsilon_{\rm v} = 0.2$) used in the simulations and listed in Table 1.

The calculations are performed on a Cray-YMP 4/64 and a Cray J90 8/512. They need about 12–16 MWords of main memory and take approximately 40 CPU-hours per simulated time unit (for the $\delta = 1/64$ models and Mach 10; the $\delta = 1/256$ models take four times as long, etc.; δ is the size of a zone on the finest grid, see Table 1).

3. Shape of the shock cone

Figure 2 shows the density distribution of five models towards the end of the simulations, emphasizing the distribution of matter on scales between one and ten accretion radii. The left Figs. 2 a, c and e, show models with a small gradient in velocity (3%), while the right Figs. b and d have large gradients (20%). Similarly to 3D models without gradients (see Ruffert 1996, and references therein), these new models do not exhibit the "flip-flop" flow visible in previous 2D simulations. The shape of the shock cones shown in Fig. 2 is fairly constant in time and remains roughly conical, contrary to the 2D flows, whose cones shifted strongly from side to side. One notices the following features when inspecting Fig. 2. The mass is distributed in a hollow shock cone (as has been reported previously) for the models with a small gradient, i.e. the density is maximal just behind the shock, while downstream from the accretor, the density is minimal along the axis. The asymmetry of the velocities in the incoming flow reflects itself in higher density maxima along the cone on the side of the lower velocities. This density asymmetry is so pronounced in the models with strong gradients (Figs. 2) that the "hollow cone" shape can be recognized only with difficulty. The line of minimum density is very irregular and is shifted from the $y = 0$-axis by several accretion radii. Already upstream of the shock a higher density is indicated by the contour of value 0.01 being detached from the shock on the positive y-axis side, while it is very close to the shock on the negative y-axis side. This density difference is easily explicable: on the side of smaller velocities gravity can act relatively more strongly to divert the flow. Thus the effective local accretion radius is larger on the side of smaller velocities and so a larger volume of matter can be gravitationally focused by the accretor. One also notices that the side of the cone with smaller densities is more irregularly shaped than the high-density side. The cavities and lumps produced by the fluctuating flow close to the accretor (at distances closer than roughly one accretion radius) can propagate more easily downstream on the side of the cone with lower densities. Since the velocity enters the accretion radius Eq. (5) via a square, one might wonder, whether the velocity is so small, that the local accretion radius is comparable to the distance of the accretor to the boundary of the computational box which is approximately at $16R_{\rm A}$. This is not the case, since inserting $v_{\rm min} = v_0/2$ (from Eq. (4)) into Eq. (5) one obtains $4R_{\rm A}$, which is a factor of 4 smaller than the distance to the computational boundary.

4. Results of models with 3% velocity gradient

4.1. Moderately supersonic accretors, Mach 3

The model denoted by IM in this work is identical to the simulation presented in Ruffert & Anzer (1995). Since for the parameters that I wanted to investigate in this paper a slightly different prescription of the velocity gradient was necessary (cf. Sect. 2.2), a comparison is called for to check how large the influence of the "tanh"-term is for small gradients $\varepsilon_{\rm v} = 0.03$. Models IM and IM* are identical except for the "tanh"-term. Fig. 3a shows a contour plot of the density in one plane for model IM, Fig. 4 shows the accretion rates of several quantities for model IM, and Fig. 5 displays the same quantities for model IM*. One notices that both the mass accretion rate as well as the specific angular momentum accreted are similar in both models for the time over which both have been calculated. I stopped the simulation of model IM* at $t \approx 8.2$ because it looked so alike to model IM. Thus I conclude that for small gradients $\varepsilon_{\rm v} = 0.03$ the difference between the "tanh"-prescription and the simple linear dependence is indeed negligible.

Models IS and IT differed only in their numerical resolution: model IT was simulated with one grid level finer, while the accretor size was very small ($R = 0.02R_{\rm A}$) compared to models IM and IM* (whose radii were 5 times larger). The density distribution of models IS and IT can be found in Fig. 3, while their accretion rates are shown in Fig. 4. Because model IT had one level of refinement more, the computational cost was larger, so the time the simulation was run is roughly half of the time of model IS. Until $t \approx 5$ both models show the same features: the mass accretion rate rises to roughly 6 units and starts fluctuating at about $t \approx 4$ time units. The specific angular momentum rises continuously until $t \approx 1$ then fluctuates around a value of roughly -0.03 while increasing the amplitudes of the fluctuations. Thus the use of 9 nested grids seems sufficient, since the calculation with 10 grids did not show any qualitative differences.

It is clear that model IT has not been evolved for long enough to obtain meaningful averages, since the fluctuation of the mass accretion rate has hardly begun when the simulation is stopped (Fig. 4). Although model IS was calculated for a longer time, the continuously decreasing mass accretion rate of model IS (Fig. 4) indicates that a stationary state has not yet been reached und so the simulation of this model should have been continued even further. However. the high computational cost precluded this. The fluctuations of the specific angular momentum, too, seem to increase with time corroborating the the statement. Thus

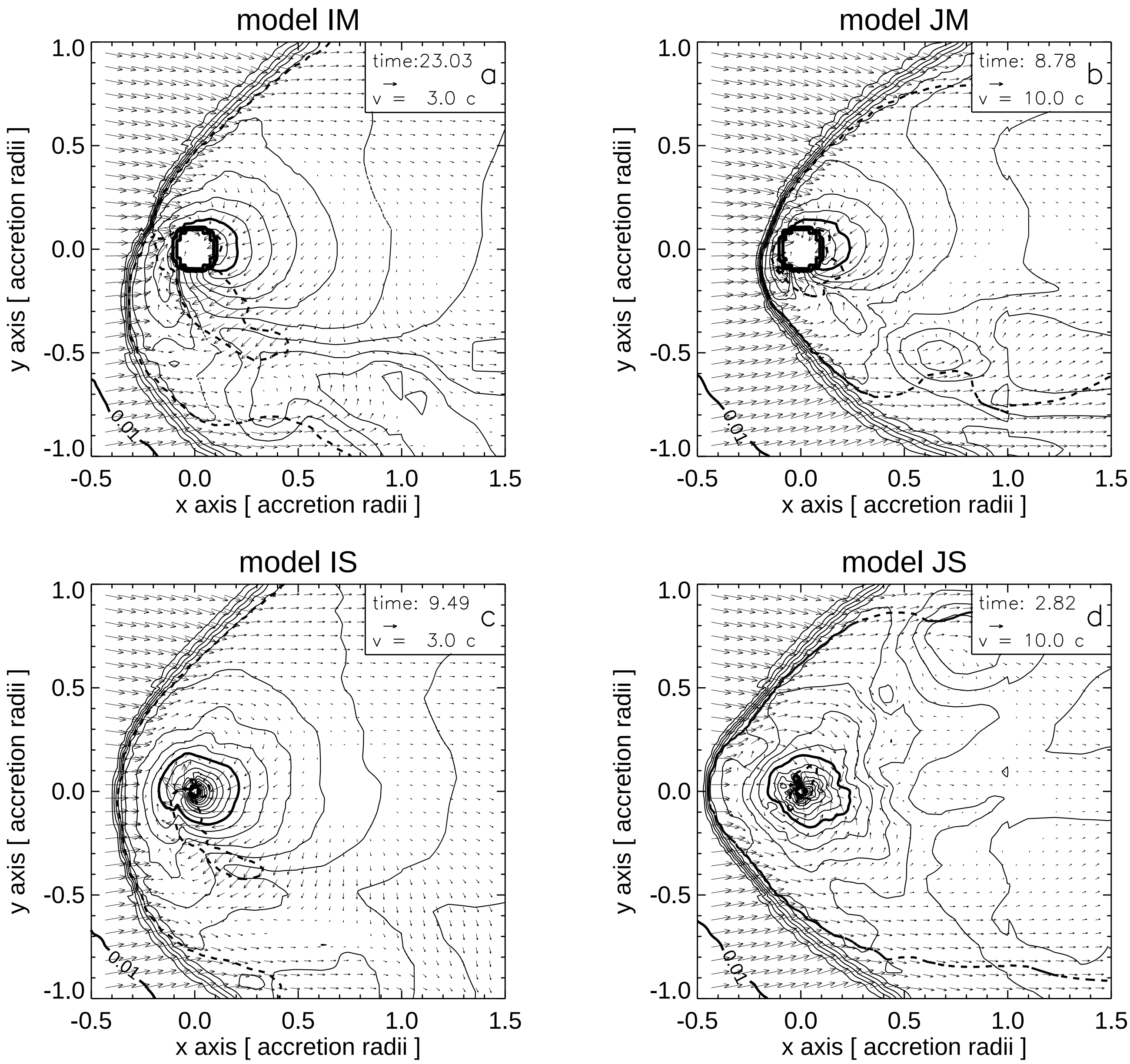

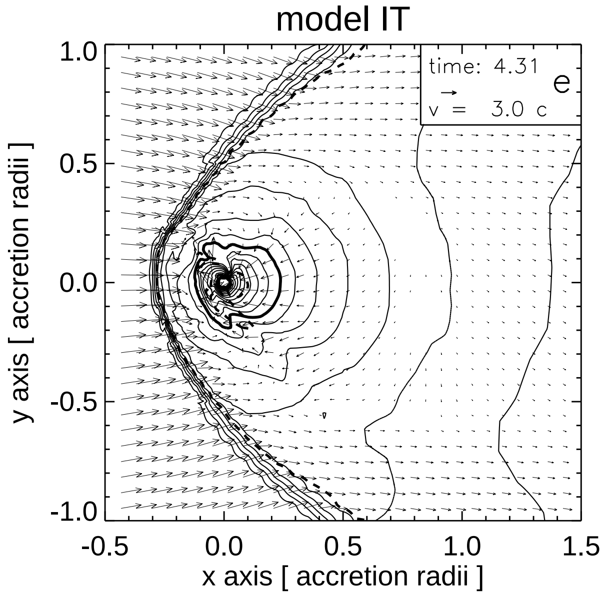

Fig. 3. Contour plots showing snapshots of the density together with the flow pattern in a plane containing the center of the accretor for all models with a velocity gradient of 3%. The contour lines are spaced logarithmically in intervals of 0.1 dex. The bold contour levels are sometimes labeled with their respective values (0.01 and 1.0). The dark shades of gray indicate a high density. The dashed contour delimits supersonic from subsonic regions. The time of the snapshot together with the velocity scale is given in the legend in the upper right hand corner of each panel.

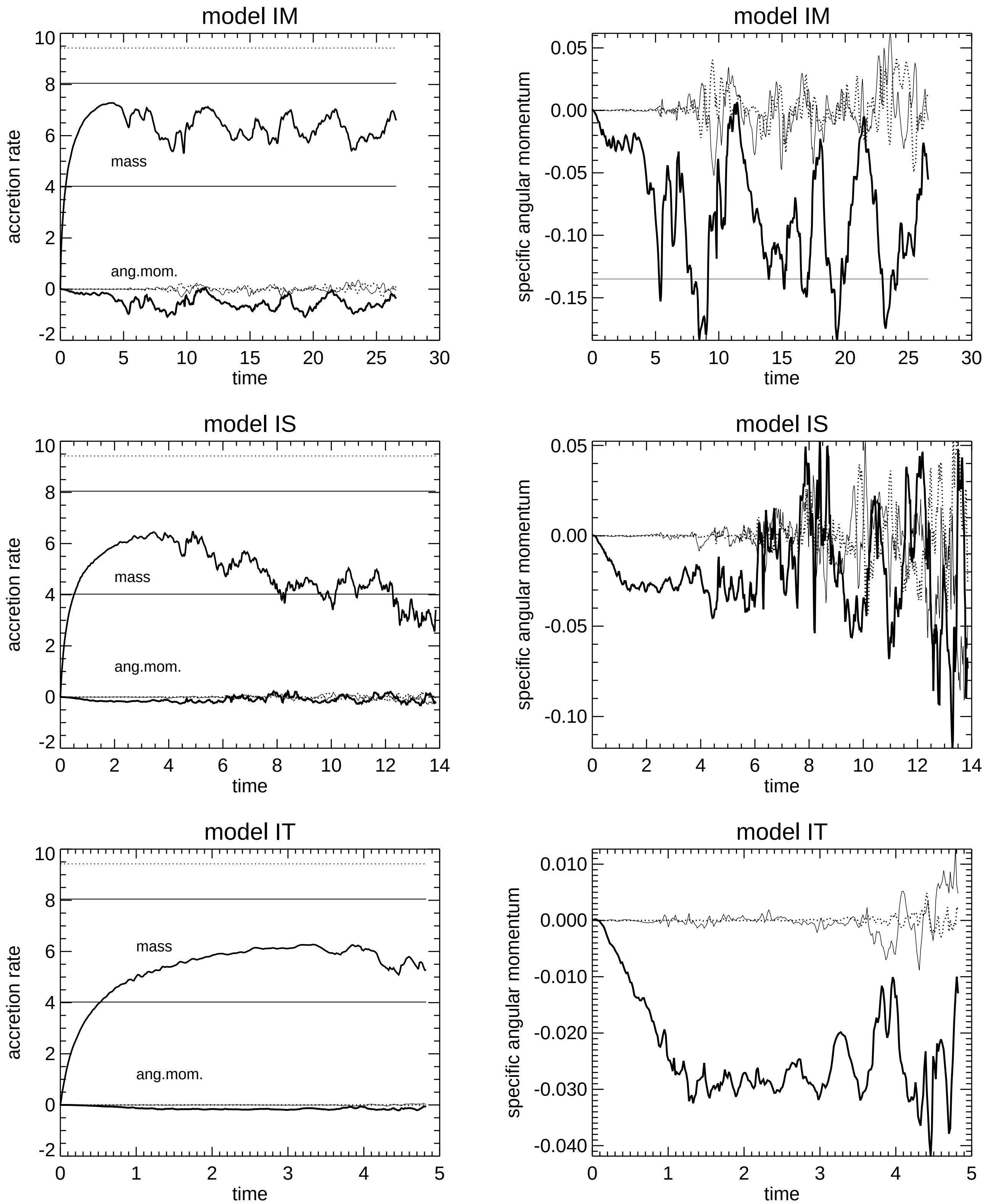

Fig. 4. The accretion rates of several quantities are plotted as a function of time for the moderately supersonic ($\mathcal{M}_\infty$=3) models IM, IS and IT with a velocity gradient of 3%. The left panels contain the mass and angular momentum accretion rates, the right panels the specific angular momentum of the matter that is accreted. In the left panels, the straight horizontal lines show the analytical mass accretion rates: dotted is the Hoyle-Lyttleton rate (Eq. (1) in Ruffert 1994a), solid is the Bondi-Hoyle approximation formula (Eq. (3) in Ruffert 1994a; Bondi 1952) and half that value. The upper solid bold curve represents the numerically calculated mass accretion rate. The lower three curves of the left panels trace the x (dotted), y (thin solid) and z (bold solid) component of the angular momentum accretion rate. The same components apply to the right panels. The horizontal line in the right Panel of model IM shows the specific angular momentum value as given by Eq. (7). It is outside the range of the plot for models IS and IT.

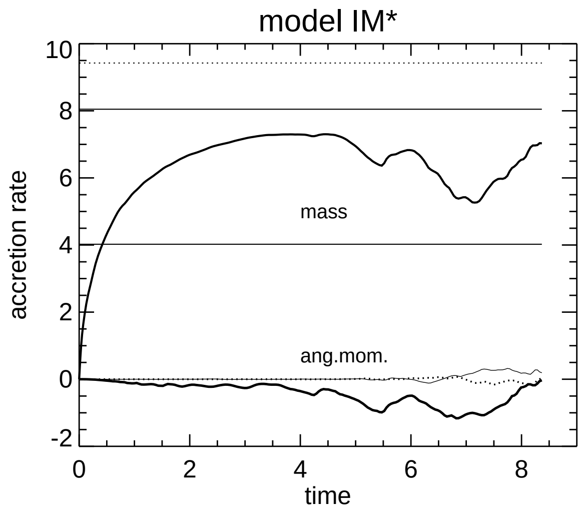

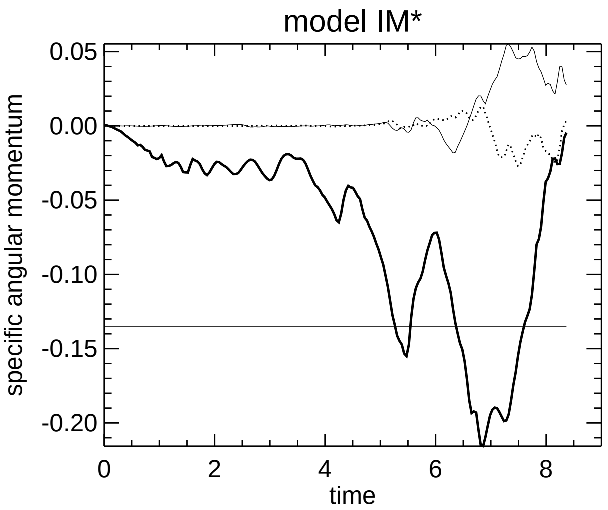

Fig. 5. The accretion rates of several quantities are plotted as a function of time for model IM*. The left panel contains the mass and angular momentum accretion rates, the right panel the specific angular momentum of the matter that is accreted. In the left panel, the straight horizontal lines show the analytical mass accretion rates: dotted is the Hoyle-Lyttleton rate (Eq. (1) in Ruffert 1994a), solid is the Bondi-Hoyle approximation formula (Eq. (3) in Ruffert 1994a) and half that value. The upper solid bold curve represents the numerically calculated mass accretion rate. The lower three curves of the left panels trace the x (dotted), y (thin solid) and z (bold solid) component of the angular momentum accretion rate. The same components apply to the right panel. The horizontal line in the right Panel shows the specific angular momentum value as given by Eq. (7).

the average quantities obtained from this model IS cannot be very exact.

Two uncertainties that could not be resolved by the single model IM presented in Ruffert & Anzer (1995), can now be answered. The first one pertained to the fact that the specific angular momentum (visible in the top right panel of Fig. 4) seemed to reach but not cross the zero-line. This seems to be a coincidence of the initial and boundary conditions, since in model IS (visible in the middle right panel of Fig. 4) the fluctuations are indeed large enough to change the sign of the specific angular momentum accreted. We will return to this point in Sect. 8.2. The second uncertainty was whether in the generic case the values of the specific angular momentum attained and exceeded the analytically estimated ones given by Eq. (7). Model IS clearly does *not* attain these values by a large margin, roughly a factor of 3 — the analytic value for model IS is the same as for model IM, since the accretor radius does not enter into Eq. (7). The smaller accretor radius seems to allow only smaller values of angular momentum to be accreted: if the lever arm (which is the radius of the accretor) is smaller the velocities have to be an appropriate amount larger (a factor of 5, roughly) to compensate. This is obviously not the case: the arrows in the left panels of Fig. 3 close to the surface of the accretor have roughly the same length. The smaller accretor sizes also have the effect that the time scale of the fluctuations of model IS are shorter than the ones of model IM (compare the right panels of Fig. 4).

The corresponding plot to the top left panel in Fig. 4 of model IM for the axisymmetric case can be found in the top left panel of Fig. 16 in Ruffert & Arnett (1994). For model IS the closest would be the top left panel of Fig. 22 in Ruffert & Arnett (1994). One can see, that while the amplitude of the fluctuations of the the z-component of the accreted angular momentum is comparable, the average of this component of the models with velocity gradients is clearly non-zero. Contrary to this, the x- and y-components fluctuate more strongly in the models without gradients, but in all models their temporal average is close to zero (see e.g. Table 1). The run, average and fluctuations of the mass accretion rate is similar in all models.

Due to the non-axisymmetric upstream boundary conditions it is not surprising that the shape of the bow shock is not symmetric either. There is an indication of this fact in the panels shown in Fig. 3 for the density distribution close to the accretor, but it is very prominent when inspecting the shock cone position further away from the accretor (see e.g. Fig. 1 in Ruffert & Anzer 1995). The temporal evolution shows the usual kinks and deformations of the shock cone that were described in the previous papers (Ruffert 1996, and references therein).

4.2. Highly supersonic accretors, Mach 10

The right panels of Fig. 3 display the density contours of models JM and JS, which are equivalent to models IM and IS, except for the different flow speed upsteam: Mach 10 for the J-models contrary to Mach 3 for the I-

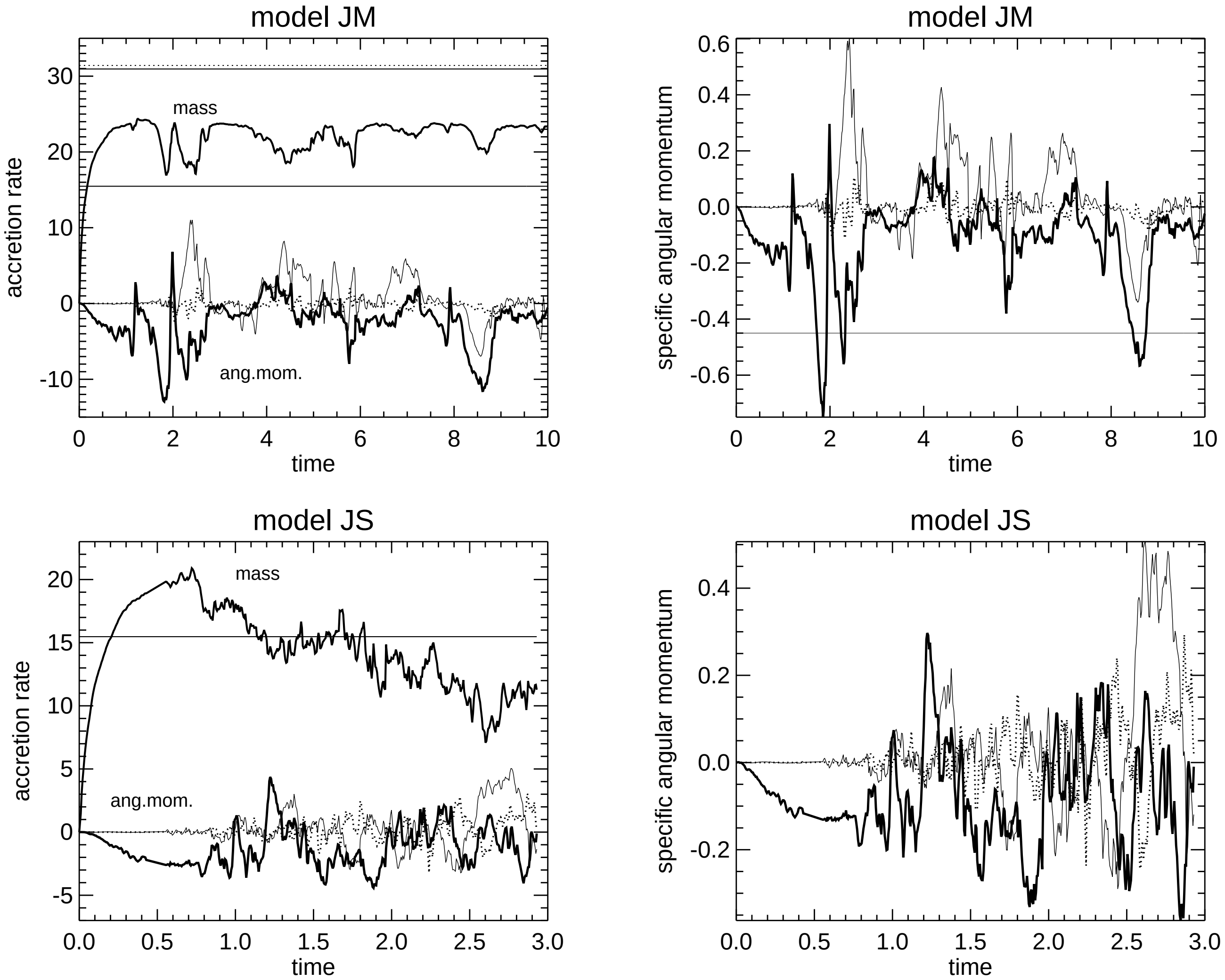

Fig. 6. The accretion rates of several quantities are plotted as a function of time for the highly supersonic ($\mathcal{M}_\infty$=10) models JM and JS with a velocity gradient of 3%. The left panels contain the mass and angular momentum accretion rates, the right panels the specific angular momentum of the matter that is accreted. In the left panels, the straight horizontal lines show the analytical mass accretion rates: dotted is the Hoyle-Lyttleton rate (Eq. (1) in Ruffert 1994a), solid is the Bondi-Hoyle approximation formula (Eq. (3) in Ruffert 1994a) and half that value. The upper solid bold curve represents the numerically calculated mass accretion rate. The lower three curves of the left panels trace the x (dotted), y (thin solid) and z (bold solid) component of the angular momentum accretion rate. The same components apply to the right panels. The horizontal line in the right Panel of model JM shows the analytic specific angular momentum value as given by Eq. (7). It is outside the range of the plot for model JS.

models. The corresponding accretion rates can be found in Fig. 6. The highly supersonic models JM and JS, too, do not converge to a quiescent steady state but show an unstable fluctuating flow pattern.

In the same way as model IM, also model JM meets and exceeds the analytically given value (Eq. (7)) of the specific angular momentum (top right panel Fig. 6, horizontal line), however only in rare, short bursts. Thus, on average, the fraction of the specific angular momentum to the analytic value is smaller than the value of the fraction of model IM (cf. Table 1 colum l_z). However, similarly to the difference between models IM and IS, the specific angular momentum of model JS is smaller still. In fact, when looking at the bottom right panel of Fig. 6, the curve for the j_z component overlaps very strongly with the curves of the other components. There is, however, still clearly a systematic shift of j_z not visible in j_x and j_y which fluctuate around zero.

The left two panels in Fig. 6 (models JM and JS) can be compared to the two top panels of Fig. 9 in Ruffert (1994b) which show the results of the equivalent models without gradients (FM and FS, respectively). The mag-

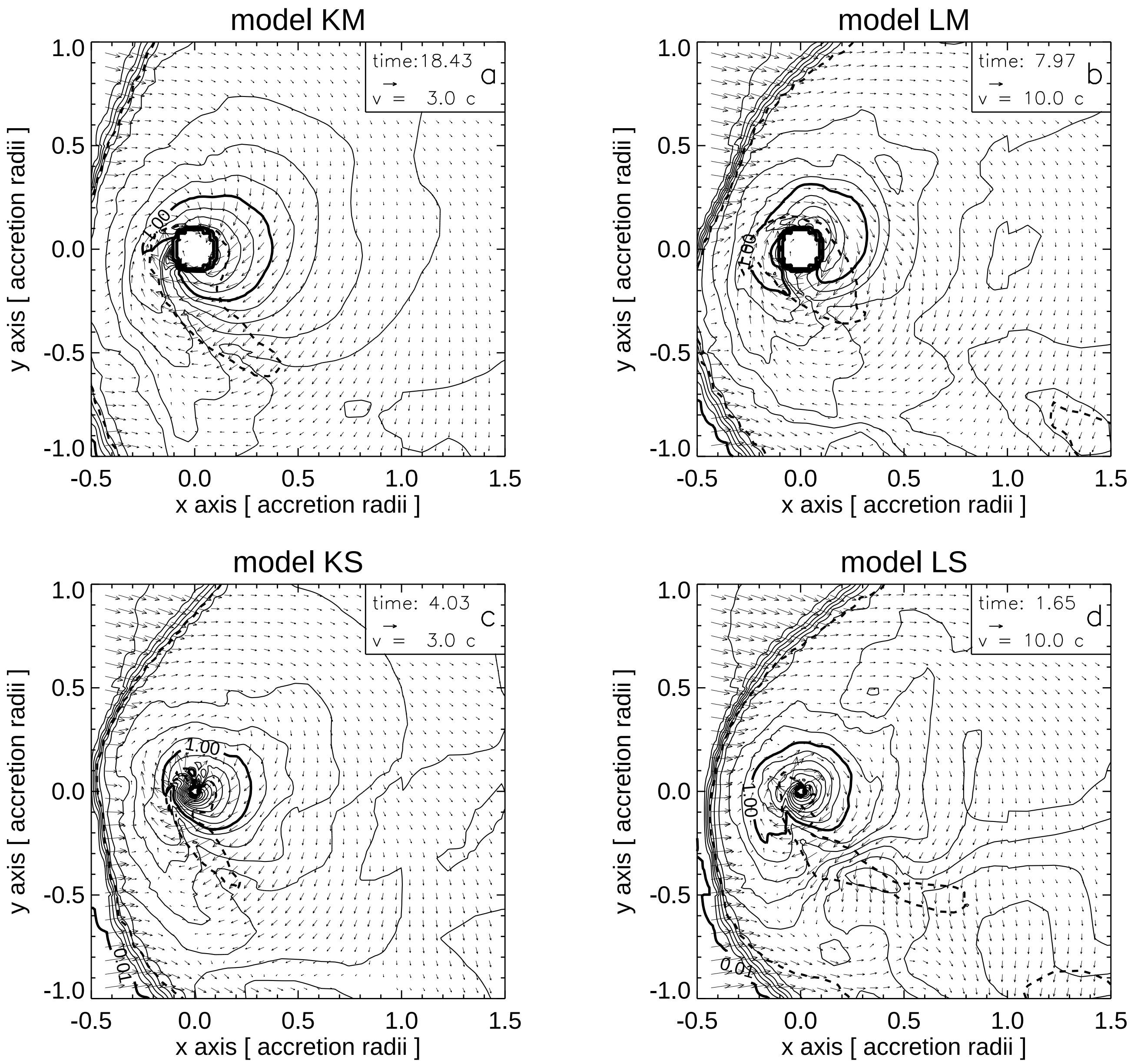

Fig. 7. Contour plots showing snapshots of the density together with the flow pattern in a plane containing the center of the accretor for all models with a velocity gradient of 20%. The contour lines are spaced logarithmically in intervals of 0.1 dex. The bold contour levels are labeled with their respective values (0.01 or 1.0). The dark shades of gray indicate a high density. The dashed contour delimits supersonic from subsonic regions. The time of the snapshot together with the velocity scale is given in the legend in the upper right hand corner of each panel.

nitude and fluctuation amplitude of the mass accretion rate are similar which is also the case for the angular momentum accretion rates (note different scale of y-axis in figures). Since the mass accretion rate of model JS seems to be steadily declining (although also fluctuating, bottom left panel in Fig. 6), this model at the time we stopped the simulation is probably still influenced by transients generated through the initial conditions. Thus the average values of e.g. the specific angular momentum, have to be used with caution.

5. Results of models with 20% velocity gradient

Models KM, KS, LM and LS break the axisymmetry very strongly since they have as boundary condition a 20% velocity gradient over one accretion radius. This asymmetry induces a strong clockwise vortex around the accretor as can be seen in Fig. 7. The sign of the velocity gradient

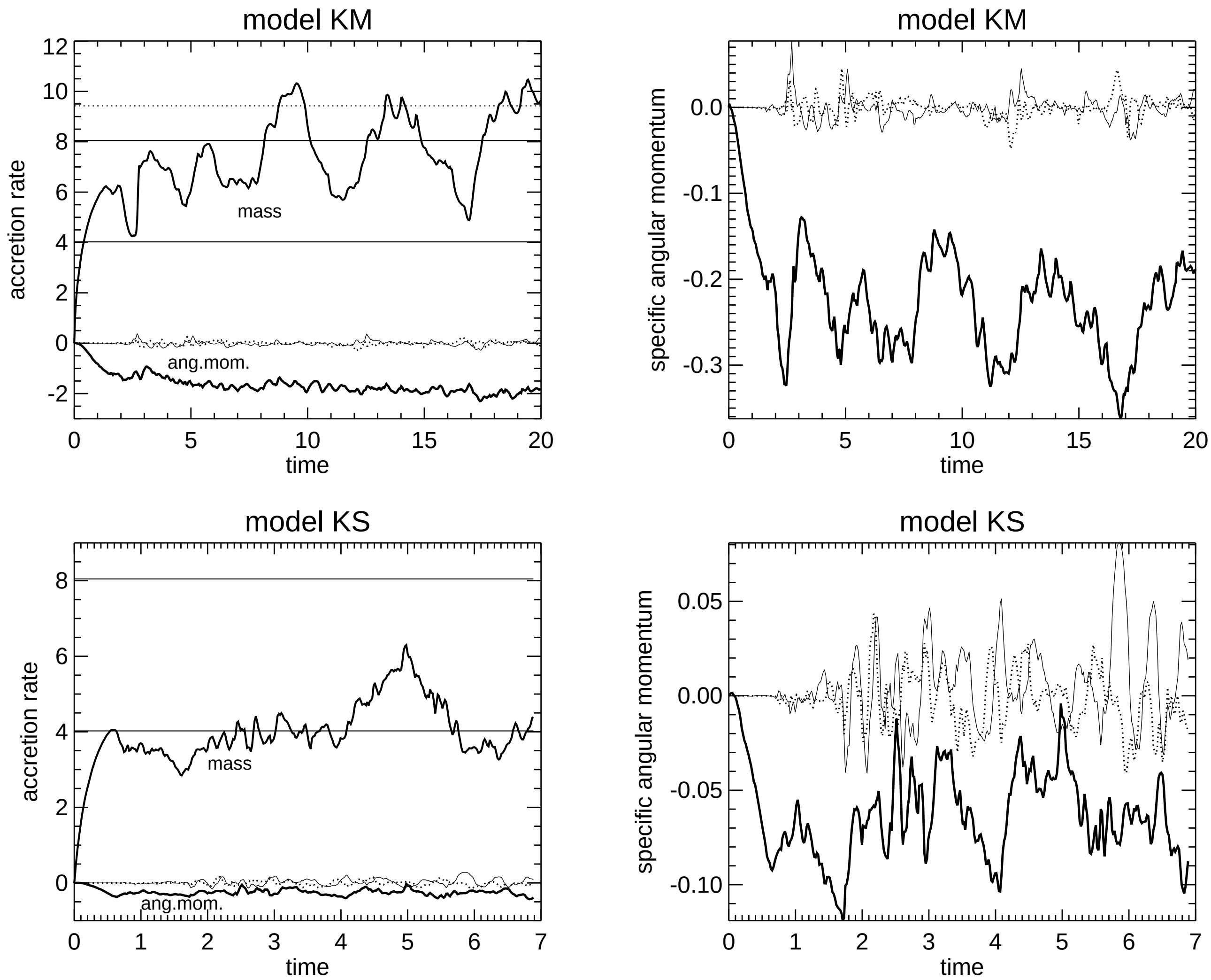

Fig. 8. The accretion rates of several quantities are plotted as a function of time for the moderately supersonic ($\mathcal{M}_\infty$=3) models KM and KS with a velocity gradient of 20%. The left panels contain the mass and angular momentum accretion rates, the right panels the specific angular momentum of the matter that is accreted. In the left panels, the straight horizontal lines show the analytical mass accretion rates: dotted is the Hoyle-Lyttleton rate (Eq. (1) in Ruffert 1994a), solid is the Bondi-Hoyle approximation formula (Eq. (3) in Ruffert 1994a) and half that value. The upper solid bold curve represents the numerically calculated mass accretion rate. The lower three curves of the left panels trace the x (dotted), y (thin solid) and z (bold solid) component of the angular momentum accretion rate. The same components apply to the right panels. The value (-0.9) of the specific angular momentum as given by Eq. (7) is outside the range of the plot for both models.

has been chosen in such a way that upstream of the accretor the higher velocities are on the negative y-side of the xy-plane (lower half of the contour plots). However, the numeric simulations confirm the sign of the analytically estimated accreted angular momentum (Eq. (7)): the vector points into the plane of the plot, which corresponds to a clockwise rotation in these contour plots. A note of caution is necessary, however: recall that Eq. (7) was derived only to lowest order in ε_v and ε_ρ, thus assuming that ε_v and ε_ρ are small compared to unity. Obviously this is questionable with the choice $\varepsilon_\mathrm{v} = 0.2$ for the models presented in this section. It is still interesting to see by how much the analytic estimates deviate from the numerical models is this extreme case.

5.1. Moderately supersonic accretors, Mach 3

The accretion rates of several quantities for models KS and KM can be found in Fig. 8. Contrary to model IM, model KM does not exhibit such strong fluctuations, thus it never even comes close (by a factor 3) to the analytically predicted value (-0.9) of Eq. (7), nor does it ever come close to the zero line. The large scale motion of the vortex around the accretor is fairly stable in time, which

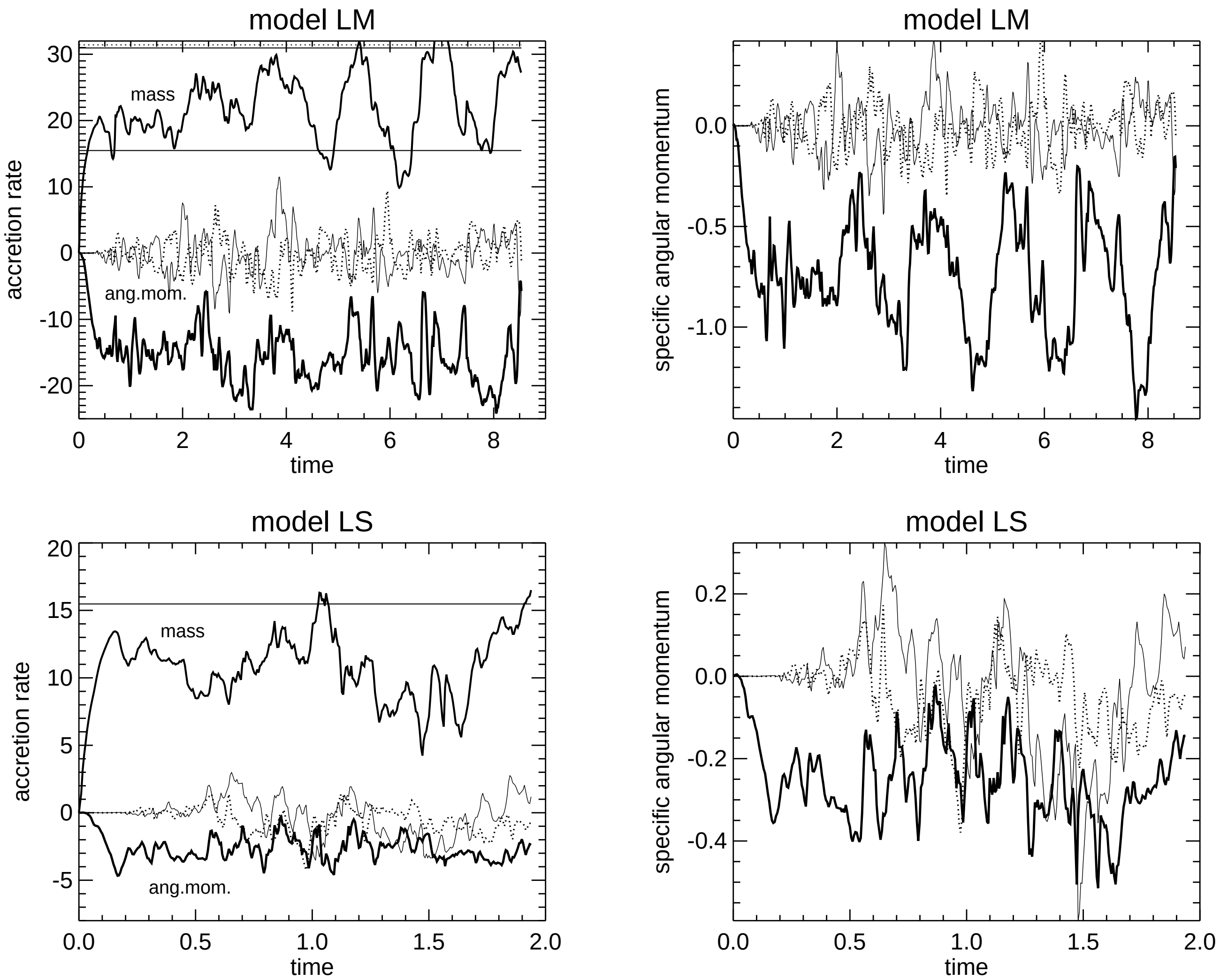

Fig. 9. The accretion rates of several quantities are plotted as a function of time for the highly supersonic ($\mathcal{M}_\infty$=10) models LM and LS with a velocity gradient of 20%. The left panels contain the mass and angular momentum accretion rates, the right panels the specific angular momentum of the matter that is accreted. In the left panels, the straight horizontal lines show the analytical mass accretion rates: dotted is the Hoyle-Lyttleton rate (Eq. (1) in Ruffert 1994a), solid is the Bondi-Hoyle approximation formula (Eq. (3) in Ruffert 1994a) and half that value. The upper solid bold curve represents the numerically calculated mass accretion rate. The lower three curves of the left panels trace the x (dotted), y (thin solid) and z (bold solid) component of the angular momentum accretion rate. The same components apply to the right panels. The value (-3.0) of the specific angular momentum as given by Eq. (7) is outside the range of the plot for both models.

explains why the fluctuations relative to the mean of the specific angular momentum are smaller in model KM than in model IM.

The fluctuations of the mass accretion rate (left panels of Fig. 8 of model KM seems to increase with time indicating that this model is still evolving in time and has not yet reached a steady mean state. These panels should be compared to the analogous panels (left in Fig. 4 for the models IM and IS. One notices that both the mean and the amplitude of the fluctuations is larger in model KM than in model IM Although the mean mass accretion rate of model KS is lower than the mean in model IS this might be a transient effect, since toward the end of model IS the mass accretion rate is of the same magnitude as in model KS. Thus for the larger accretors (M-models) the vortex allows more mass to be accreted, while for the small accretors (S-models) the difference is negligible. Both models KM and KS have one difference in common compared to model IM and IS respectively: the unstable flow, which manifests itself e.g. via a fluctuating mass accretion rate, begins much faster for the models with a large gradient, models KM and KS. Also the large-scale fluctuations of the specific angular momentum

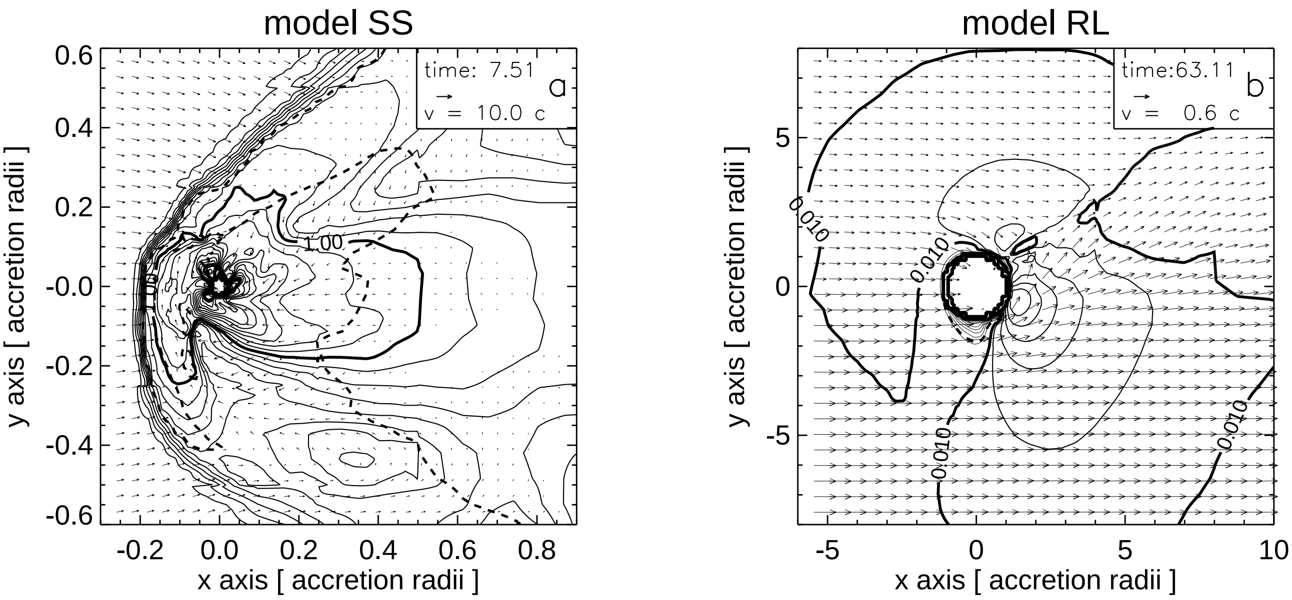

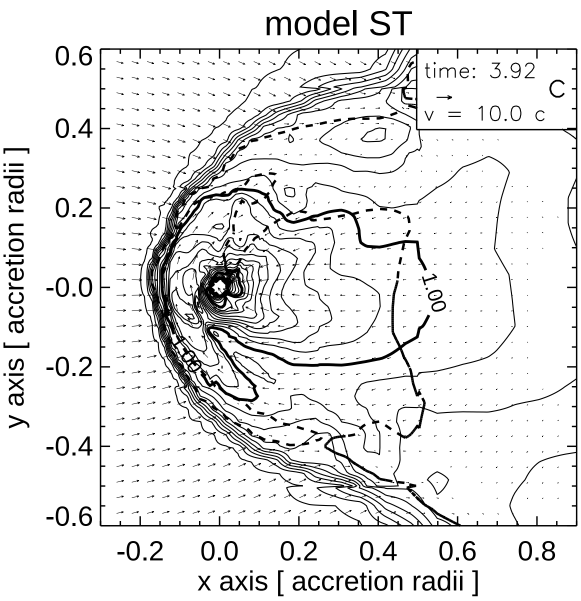

Fig. 10. Contour plots showing snapshots of the density together with the flow pattern in a plane containing the center of the accretor for models SS, ST and RL. The contour lines are spaced logarithmically in intervals of 0.1 dex for panels a and c, while panel b shows contours in intervals of 0.02 dex. The bold contour levels are labeled with their respective values. The dark shades of gray indicate a high density. The dashed contour delimits supersonic from subsonic regions. The time of the snapshot together with the velocity scale is given in the legend in the upper right hand corner of each panel.

appear at roughly $t \approx 1$ in models KM and KS, while it takes until $t \approx 4$ in models IM and IS.

5.2. Highly supersonic accretors, Mach 10

The accretion rates of several quantities for the highly supersonic models LM and LS are shown in Fig. 9. The fluctuation amplitude of the mass accretion rate of model LM is larger than both the amplitudes of model JM (top left panel in Fig. 6) and of model FM (top left panel of Fig. 9 in Ruffert 1994), however the mean seems roughly equal. On the whole model LM looks more unstable and active than the models JM and FM with small or no gradients. The mass accretion rate of model LS does not seem to decline constantly during the first two time units as was the case for model JS.

The trend that the model with the smaller accretor (in this case model LS compared to model LM) has the z-component shifted closer to the zero line is repeated also for the highly supersonic models with large gradients. The fluctuations around the mean of the z-component has roughly the same amplitude and frequency as the fluctuations of the x and y-components around zero.

6. Results of models with index 4/3

As a check for the numerics two models were run with the same physical initial and boundary conditions, but differing in resolution of the accretor: model SS used 9 grids,

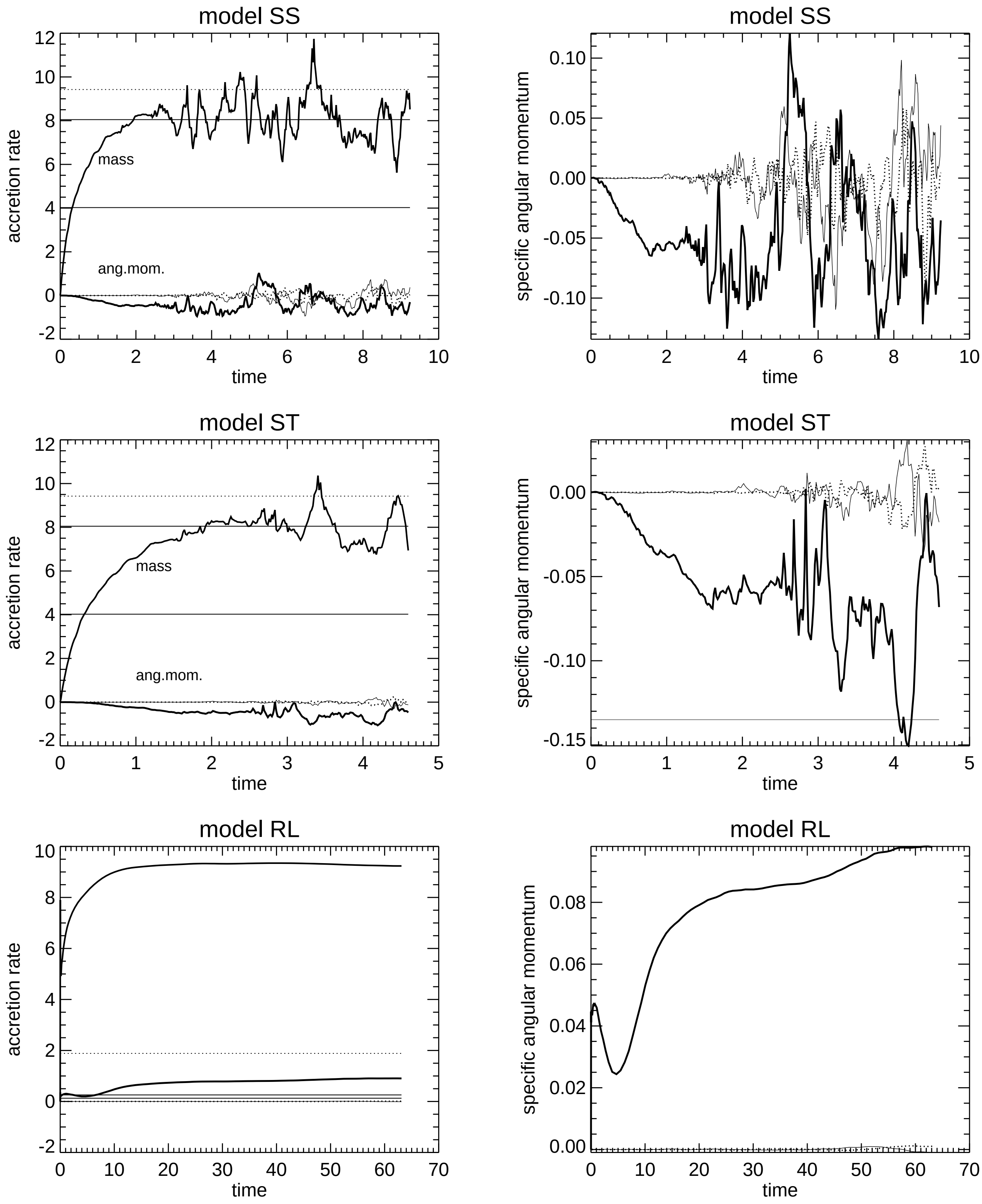

Fig. 11. The accretion rates of several quantities are plotted as a function of time for models SS, ST and RL. The left panels contain the mass and angular momentum accretion rates, the right panels the specific angular momentum of the matter that is accreted. In the left panels, the straight horizontal lines show the analytical mass accretion rates: dotted is the Hoyle-Lyttleton rate (Eq. (1) in Ruffert 1994a), solid is the Bondi-Hoyle approximation formula (Eq. (3) in Ruffert 1994a) and half that value. The upper solid bold curve represents the numerically calculated mass accretion rate. The lower three curves of the left panels trace the x (dotted), y (thin solid) and z (bold solid) component of the angular momentum accretion rate. The same components apply to the right panels. The horizontal line in the right Panel of model ST shows the specific angular momentum value as given by Eq. (7). It is outside the range of the plot for models SS and RL.

model ST used 10 grids (cf. Table 1 for the other parameters). The two left panels of Fig. 10 show contour plots of the density distribution, while the acretion rates of mass and angular momentum can be found in Fig. 11. Especially the temporal evolution of the accretion rates confirm that also for $\gamma = 4/3$ using grids to 9 levels deep is sufficient: within the time in which the two models SS and ST overlap, the mass accretion rate and the angular momentum accretion agree to within a few percent.

Models SS and ST (Fig. 11) are equivalent to models IS and IT, (Fig. 4) so a comparison should show what effects are due to the different adiabatic index γ. Additionally, model SS can be compared to model CS shown in Fig. 6 of Ruffert (1995). Both the mean and the amplitude of the mass accretion rate of model SS are similar to the ones of model CS, and even the angular momentum accretion fluctuations do not show any striking difference. When comparing model SS to model IS one notices that the mass accretion rate proceeds in a much more unstable way in model SS. The rate of mass accretion as well as the specific angular momentum of the z-component are larger in model SS. So much so, that in a short burst model ST actually reaches the analytically estimated value (middle right panel of Fig. 11) contrary to model IS or IT. Thus we conclude that the models with $\gamma = 4/3$ accrete in a less stable way than their $\gamma = 5/3$ equivalents, which is the opposite from what had been observed in the simulations without gradients (Ruffert 1995 and references therein). More $\gamma = 4/3$ models are necessary before any more systematic statements can be made.

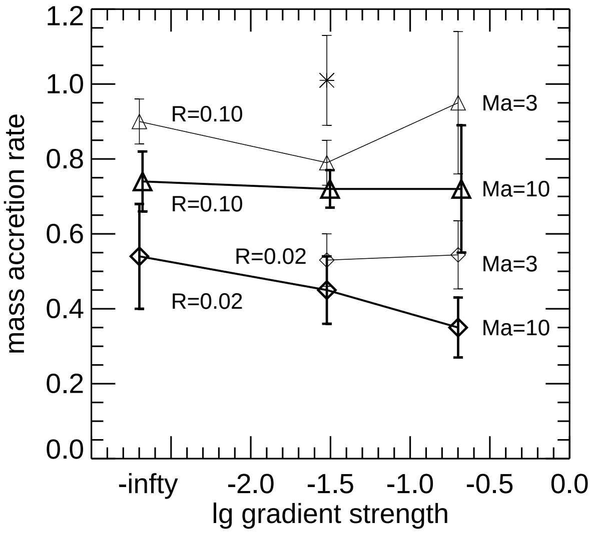

Fig. 12. Mass accretion rates (units: $\dot{M}_{\rm BH}$) are shown as a function of the strength of the velocity gradient: 20% and 3% are the results from this work, while the values for models without gradient (at the x-axis position "-infty") are taken from Ruffert (1994a) and Ruffert & Arnett (1994). Diamonds ($\diamond$) denote models in which the accretor has a radius of 0.02 $R_{\rm A}$, triangles ($\triangle$) models with 0.1 $R_{\rm A}$. The large bold symbols belong to models with a speed of $\mathcal{M}_\infty = 10$, while the smaller symbols belong to models with $\mathcal{M}_\infty = 3$. The accretor radius and Mach number are also written near each set of points. All models have $\gamma = 5/3$, except for the "star" which denotes model SS. The error bars extending from the symbols indicate one standard deviation from the mean (S in Table 1). Some points were slightly shifted horizontally to be able to discern the error bars.

7. Results of model RL

Model RL is extreme in two aspects: firstly the radius of the accretor is one accretion radius in size and thus very large, and secondly the flow speed upstream of the accretor is subsonic, Mach 0.6. Additionally the gradient was chosen to be large (0.2). These conditions, although extreme, might, however, be present in stellar binary systems with a wind from a nova (K. Schenker, personal communication), thus the model is not totally academic, but one has to take care in relating the physical size of the stars to the radius of the accretor used in the simulations. The contour plot showing the density distribution together with the instantaneous velocities is shown in Fig. 10b, while the corresponding accretion rates are shown in the bottom panels of Fig. 11. The large scale of the contour plot shows the velocity gradient clearly.

After $t \approx 10$ time units model RL has practically reached a stationary state in which mass is accreted at a constant rate (bottom left panel in Fig. 11. This behaviour as well as the value of the mass accretion rate is very similar to model SL in Ruffert (1994b; top left panel of Fig. 2). The small fluctuations of the angular momentum visible in model SL are initial transients due to a small (3%) perturbation of the initial density distribution. I did not perturb the density in any model presented in this paper. This model RL is the only model presented in this work that reaches a constant state, which is probably due to the subsonic flow, sa has been reported elsewhere for models without gradients (e.g. Ruffert 1995).

The main difference concerning accreted quantities between model RL and all other models in this paper is the sign of the accreted angular momentum: it is positive (cf. Fig. 11), while the z-component of the angular momentum accreted of all other models is negative (see also Table 1). This is probably due to the fact that an accretor with such a large radius accretes mainly via its large geometric cross section, and not following the classic Bondi-Hoyle-Lyttleton scenario involving gravitational focussing, accretion mainly from the downstream side, etc. (the low Mach number might also play a role). Thus the matter is directly absorbed from the incoming stream without first being "processed" though a shock, taking with it the angular momentum it had upstream: this produces a anti-clockwise rotating vortex around the accretor (contrary to the clockwise vortex mentioned in Sect. 5).

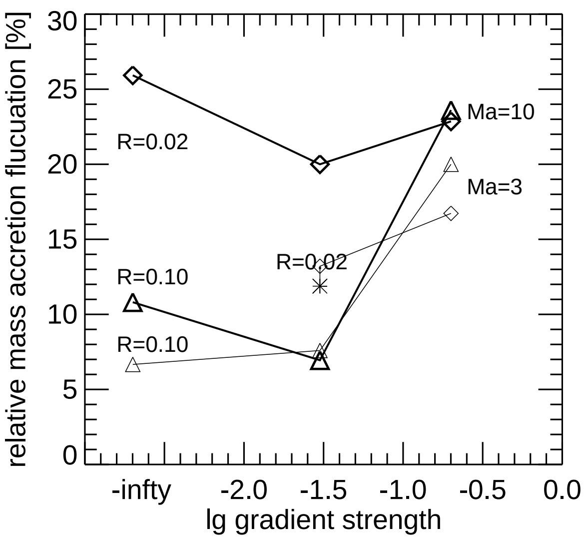

Fig. 13. The relative mass fluctuations, i.e. the standard deviation S divided by the average mass accretion rate $\overline{\dot{M}}$ (cf. Table 1), is shown as a function of the strength of the velocity gradient: 20% and 3% are the results from this work, while the values for models without gradient (at the x-axis position "-infty") are taken from Ruffert (1994a) and Ruffert & Arnett (1994). Diamonds ($\diamond$) denote models in which the accretor has a radius of 0.02 R_A, triangles ($\triangle$) models with 0.1 R_A. The large bold symbols belong to models with a speed of $\mathcal{M}_\infty = 10$, while the smaller symbols belong to models with $\mathcal{M}_\infty = 3$. All models have $\gamma = 5/3$, except for model SS (with $\gamma = 4/3$) denoted by a star ($*$).

8. Analysis of Results

8.1. Mass accretion rate

The mass accretion rates obtained in this work for all models except IT, RL, and ST are collected in Fig. 12 together with the amplitude of their fluctuations (one standard deviation). This figure indicates that, to first order, the mass accretion rate is independent of ε_v, even for the large $\varepsilon_\mathrm{v} = 0.2$. Although the mean mass accretion rate does vary slightly with Mach number and accretor radius, even in units of $\dot{M}_\mathrm{BH}$, the variation of the rates across different velocity gradients ε_v remains within the fluctuations of the unstable flow. This is only in partial agreement with Fig. 1. Up to $\varepsilon_\mathrm{v} = 0.1$ no variation is expected from Fig. 1 if all mass in the accretion cylinder is actually accreted (which is an assumption that enters when deriving Eq. (6), etc.). However, since the mass accretion rate seems to remain unchanged even for the models with $\varepsilon_\mathrm{v} = 0.2$ (contrary to Fig. 1), we conclude that for these large velocity gradients not all matter in the accretion cylinder is accreted any longer.

The relative mass fluctuations, i.e. the standard deviation S divided by the average mass accretion rate $\overline{\dot{M}}$ (cf. Table 1), have been collected in Fig. 13. Although some models cluster around a relative fluctuation of 5%–10% while others are around 15%–25%, it is not clear which combination of parameters is responsable for this division.

Two general statements can be made. When, starting from axisymmetric models, slightly increasing in the velocity gradient to a few percent, the relative accretion rate fluctuation either remains unchanged or decreases. In the axisymmetric case, any eddy will produce a fluctuation of the accretion rates. As long as the velocity gradient is small, the vortex generated by the the incoming angular momentum around the accretor is of the same strength as the eddies and it might be able to stabilize the flow around the accretor. When further increasing the velocity gradient the relative fluctuations increase strongly. So the stabilizing effect is lost indicating that the vortex itself contributes to the eddies and the fluctuations.

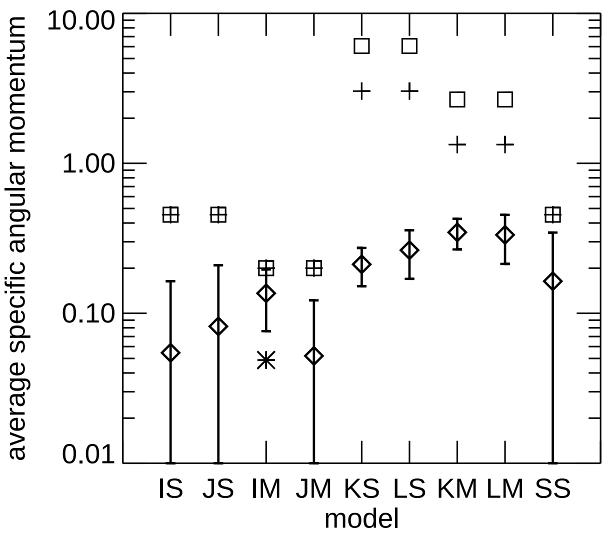

Fig. 14. The average specific angular momentum (units: l_s, Kepler velocity vortex at surface of accretor, as given by Eq. (10)) is shown for most models by diamond symbols (l_z in Table 1). The "error bars" extending from the symbols indicate one standard deviation from the mean (σ_z in Table 1). The long error bars extending to the bottom axis are an indication that the fluctuations of the respective model are so large, that the specific angular momentum changes sign from time to time. The plus signs above the diamonds indicate the specific angular momentum j_z according to the Shapiro & Lightman (1976) prescription, Eq. (7), while the squares denote the values j_z taken from the semi-numerical estimate, Eq. (9) and Fig. 1. All models have $\gamma = 5/3$, except for model SS ($\gamma = 4/3$). The star ($*$) at the position of IM is the value taken from Ishii et al. (1993) (see text in Sect. 8.3)

8.2. Specific angular momentum

Assuming a vortex flowing with Kepler velocity V just above the accretor's surface with radius $R_\star$, the specific angular momentum of such a vortex is

$$l_{\mathrm{s}} = R_\star V = \sqrt{R_\star/R_{\mathrm{A}}}\mathcal{M}_\infty R_{\mathrm{A}} c_\infty/\sqrt{2} \quad . \tag{10}$$

The term $\sqrt{2}$ has erroneously been omitted in my previous works (e.g. Ruffert, 1996). Although for short periods of time the specific angular momentum can exceed l_{s}, it is difficult to imagine how accreted matter can *on average* (temporal) exceed this value. This implies that smaller objects (smaller $R_\star$) can accrete only smaller specific angular momenta, which goes to zero like $\sqrt{R_\star}$.

In Fig. 14, I plot for several models the numerically obtained quantities l_{z} along with the amplitude of the fluctuations (one standard deviation, σ_{z}), which can be found in Table 1. These are plotted in units of l_{s} (Eq. (10)). Additionally, above the diamonds denoting the above mentioned ratio $l_{\mathrm{z}}/l_{\mathrm{s}}$, I plot, using plus-signs, the values that one expects for the analytically estimated quantity j_{z} from Eq. (7) and denoting by squares, j_{z} from the semi-numerical estimate, Eq. (9).

Several trends can easily be noticed in Fig. 14. Model JM seems to be well below the general trend, indicating that the simulation was not evolved for long enough; I will not include this model in the following discussion. The four "K" and "L" models form a fairly homogeneous group accreting roughly 0.3 of the Kepler specific angular momentum. For the "I"- and "J"-models this fraction is roughly 0.1, thus confirming that for models with smaller gradients, the vortex around the accretor is less pronounced. These two groups vary less among themselves than the variation one would expect if the analytical estimates Eq. (7) (plus signs) or Eq. (9) (squares) were valid. Thus, when estimating the specific angular momentum one should be guided by the Kepler-values Eq. (10). When applying Eq. (7) one should bear in mind the allowable parameter range: small gradients, supersonic flow and small accretors. A good counter example is model RL, which exhibits a constant state and the sign of the accreted angular momentum is opposite to Eq. (7).

The smaller lever arm acting in models with smaller accretors is included in Eq. (10). Still, the "S"-cases have a slightly smaller value of $l_{\mathrm{z}}/l_{\mathrm{s}}$ compared to the "M"-cases. The reduction is, however, not uniform for all models; the models with large gradients show reductions of at most a factor of 2, while the other models have a factor of 3. So small accretors impede high specific angular momentum accretion in some additional way than only via their smaller lever arm. At the distance of the surface (= radius of the accretor), matter seems to move in eddies at some fraction of the Kepler-speeds. This fraction is dependent more on the velocity gradient ε_{v} than on the size of the accretor or the Mach number. Recall, that from Fig. 1 one would expect the models with large gradients ("K" and "L") to accrete specific angular momenta a factor of 2 larger than the analogous models with small gradients ("I" and "J"). This is in contradiction to what is shown in Fig. 14, confirming again that the assumption of accreting everything from the accretion cylinder is not correct for large gradients.

When the fluctuations of the specific angular momentum are larger than its mean, then the accreted angular momentum can change sign, indicating a reversal of the rotation direction of a disk around the accretor. This will most easily be attained for models with a small gradient, since the fluctuations need not be large in these cases. These models have their "error bars" extending completely down to the x-axis in Fig. 14. For one of these models, model SS, Fig. 15 shows the reversal of the disk surrounding the accretor. The "normal" rotation direction is shown in Fig. 15e for model KS which has a large gradient $\varepsilon_{\mathrm{v}} = 0.2$. From the bottom right panel in Fig. 8 one can see that the specific angular momentum never changes sign indicating a strong regular flow around the accretor. This is visible in Fig. 15e: the disk (region of azimuthal flow) extends to a distance of at least 0.3 R_{A} and is, however, slightly eccentric. In contrast, the disk around the models with small gradient, e.g. model SS, is smaller: roughly 0.1 R_{A}. Figs. 15a to d show this small disk alternating between clockwise and anti-clockwise rotation. Shocks appear when matter originating outside the disk is accreted in the opposite direction of the current disk rotation, e.g. shortly after the disk has been counterrotating (in Fig. 15a), matter from downstream forces the disk to rotate in anti-clockwise direction (in Fig. 15b). In this figure a shock is visible at $(x \approx -0.05, y \approx -0.05)$: note the velocity discontinuity, the change from supersonic to subsonic (dashed line) and the increase in density (darker shades) when going with the flow in anti-clockwise direction at $(x \approx -0.05, y \approx -0.05)$.

Shocks imply generation of entropy, thus if shocks appear more often when the direction of rotation of the disk is reversed one would expect that matter with higher specific entropy is accreted during phases when the specific angular momentum of the matter changes sign. To find such a possible correlation, I draw in Fig. 16 a dot connecting the two quantities for every second time step of the numerical simulation. This was done only for the four models JM, JS, IS, and SS which exhibited a change in sign of the specific angular momentum (see e.g. Fig. 14). The two models JM and IS (Fig. 16a and c) have an only small intrinsic scatter of the specific entropy accreted (roughly 10%) indicating that the fluctuations visible in Figs. 4 and 6 do not generate equally fluctuating shock structures. For model JM the entropy does not at all seem to correlate with the angular momentum, while for model IS a marginal indication exists that the specific entropy is slightly higher for larger (=more positive) specific angular momenta. On the other hand, the highest entropies appear at the most negative momenta. In con-

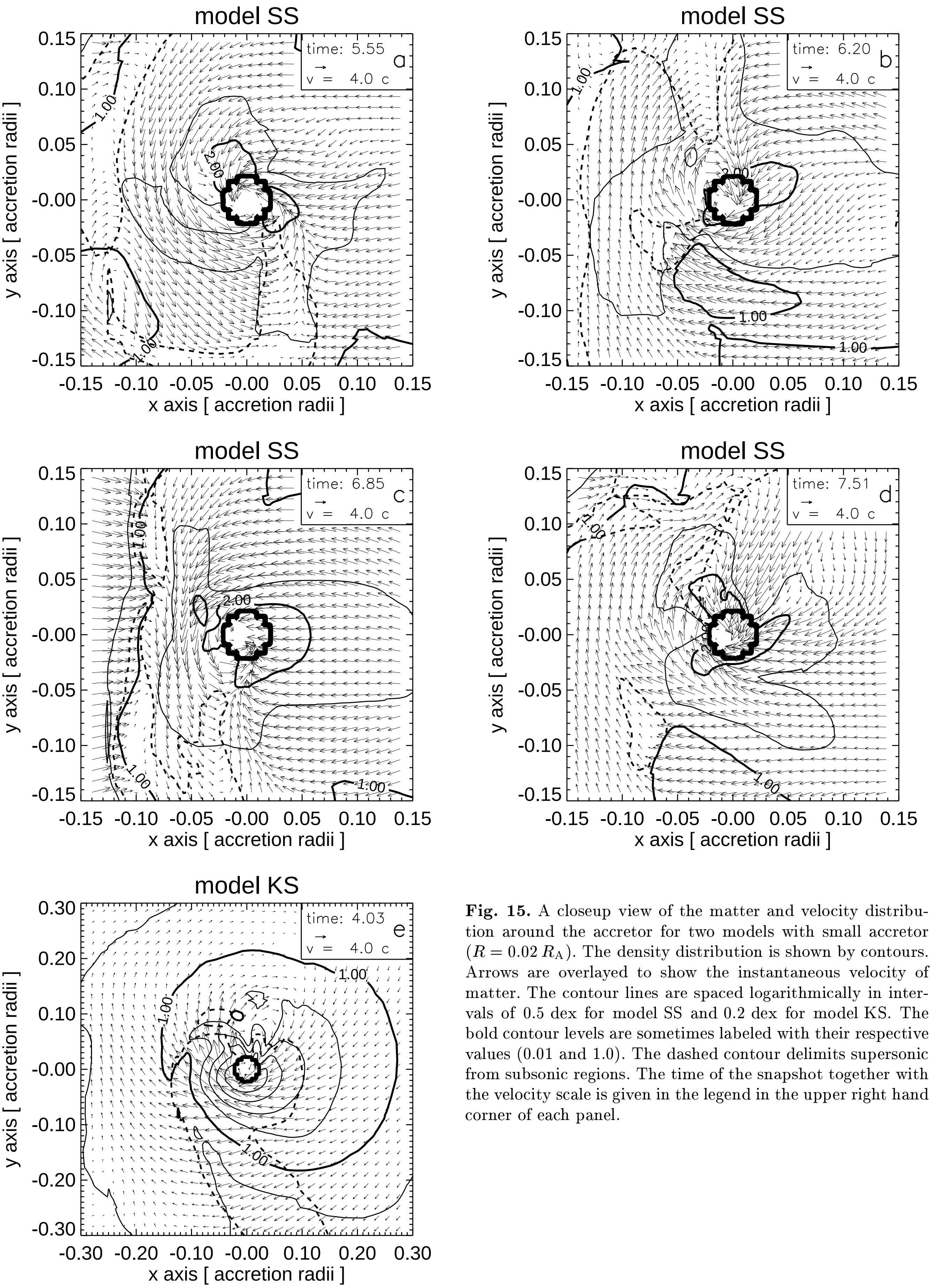

Fig. 15. A closeup view of the matter and velocity distribution around the accretor for two models with small accretor ($R = 0.02\,R_{\rm A}$). The density distribution is shown by contours. Arrows are overlayed to show the instantaneous velocity of matter. The contour lines are spaced logarithmically in intervals of 0.5 dex for model SS and 0.2 dex for model KS. The bold contour levels are sometimes labeled with their respective values (0.01 and 1.0). The dashed contour delimits supersonic from subsonic regions. The time of the snapshot together with the velocity scale is given in the legend in the upper right hand corner of each panel.

trast, models JS and SS exhibit a relatively large scatter of the specific entropy (roughly 40% and 25%, respectively) and fairly clear correlations. In model JS (Fig. 16b) high entropy material is accreted preferentially when the angular momentum is small (around zero). This result confirms what has been described at the beginning of this paragraph. The correlation in Model SS (Fig. 16d) is different again: no material with low specific entropy (less than say 4.9) is accreted when the specific angular momentum is positive. Thus the disk seems to be in constant turmoil (with many shocks) when the disk rotates in anti-clockwise direction (which is contrary to the "normal" direction, cf. beginning of this Sect. 8.2). However, when the disk rotates in clockwise direction both high and low entropy material (more or less than 4.9) is present.

In Fig. 17 the rate at which mass is accreted is plotted versus the specific angular momentum. Analogously to the differing correlations of the entropy, the four models JM, JS, IS, and SS display different behaviours. The correlation in model SS is clearest: the mass accretion rate is highest when the specific angular momentum is around zero and the rate decreases for more positive and more negative values of the specific angular momentum. A similar, but less clear, trend can be discerned for model JM (Fig. 17). Obviously, when the flow does not rotate around the accretor it falls down the potential to the surface of the accretor and can thus be absorbed more efficiently.

The maximum rate at which mass is accreted also decreases with increasing magnitude of specific angular momentum (independent of sign) in models JS and IS (Figs. 17b and c). However, the smallest mass accretion rates are scattered fairly uniformly along all momenta.

8.3. Comparison with previous works

Two of the previously published *two*-dimensional simulations mentioned in the introductory chapter Sect. 1 investigate a velocity gradient (as was done here); Taam & Fryxell (1989) and Anzer et al. (1987). The most important parameters of the first work are: the radius of the accretor is $R = 0.037\,R_{\rm A}$, the adiabatic index is $\gamma = 4/3$, the velocity gradient is $\varepsilon = 0.005$ or $\varepsilon = 0.0625$, with a Mach number of $\mathcal{M} = 4$ or $\mathcal{M} = 12$. Thus a model most similar to these conditions is model SS (cf. Table 1). When comparing the top two panels of Fig. 11 with the equivalent Figs. 10 and 11 in Taam & Fryxell (1989) one notices one main difference: model SS does not show the "flaring events" described by Taam & Fryxell (1989). These flaring events are due to the collapse of otherwise fairly stable disks around the accretor. In quasi-regular intervals the disk changes its direction of rotation and during these inversions the mass of the disk is accreted. This yields short episodes of very high accretion rates, termed flaring events by Taam & Fryxell (1989). In model SS the disk is much less stable than in Sequence 2 of Taam & Fryxell (1989), consequently the buildup and collapse of the disk is much more eratic, so no flaring events of the same magnitude as in Taam & Fryxell (1989) is seen in model SS. That the disk is so stable in the simulation by Taam & Fryxell (1989) is due to the fact that their calculation is two-dimensional, contrary to the three-dimensional models presented here. Once a disk is formed in a two-dimensional calculation hardly any matter can be accreted in radial direction. In three-dimensions, however, matter can still be accreted via the polar caps even if is disk is present in the equatorial plane. If this matter is focussed from above and below the disk, it can also act to disrupt the integrity of the disk, shortening the lifetime of the disk in three-dimensional calculations.

The most important parameters of the Anzer et al. (1987) work are: the radius of the accretor is $R = 0.14\,R_{\rm A}$, the adiabatic index is $\gamma = 1.5$, the velocity gradient is $\varepsilon = 0.3$ and the Mach number is $\mathcal{M} = 3$. Models IM or SS from the present work most closely resemble these parameters. In Sect. 4 of Anzer et al. (1987) they report finding a ratio of 0.22 between the numerically obtained (SPH simulation with 7500 particles) specific angular momentum and the analytically estimated value. This value is within a factor of two of the results shown in Fig. 14.

Of the five previously published *three*-dimensional simulations mentioned in the introduction, we will concentrate our comparison to the results of Ishii et al. (1993). In the other cases the numerics is very coarse or questionable, e.g. few zones or particles, local time stepping not appropriate to the problem, etc. The parameters which were used in the "3D velocity inhomogeneous case" of Ishii et al. (1993) are the following. The radius of the accretor is $R = 0.125\,R_{\rm A}$, the adiabatic index is $\gamma = 1$ (isothermal), the velocity gradient is $\varepsilon = 0.1$ and their Mach number is $\mathcal{M} = 3$. No model described in the present paper (cf. Table 1) has such a low adiabatic index, but the other parameters are most closely covered by model IM or KM. The value that Ishii et al. (1993) obtain numerically (24% is -0.11 devided by -0.45, these values are taken from Sect. 3.5 in Ishii et al. 1993) is represented by a star ($*$) in Fig. 14. Their value (24%) must be used with caution, since their model has an adiabatic index of $\gamma = 1$ and their numerical resolution of the accretor is only two zones. Extrapolating from the models presented in this paper, I would expect a higher value, since the average specific angular momentum of model SS (smaller γ) is larger than of model IS (larger γ), and the models with larger accretors ("M"-models) are larger still.

9. Conclusions

For the first time a comprehensive numerical *three*-dimensional study is presented of wind-accretion with a velocity gradient using a high resolution hydrodynamic code. I vary the following parameters: Mach number of the relative flow (Mach 3 and 10), strength of the velocity gradient perpendicular to this flow (3% and 20% over

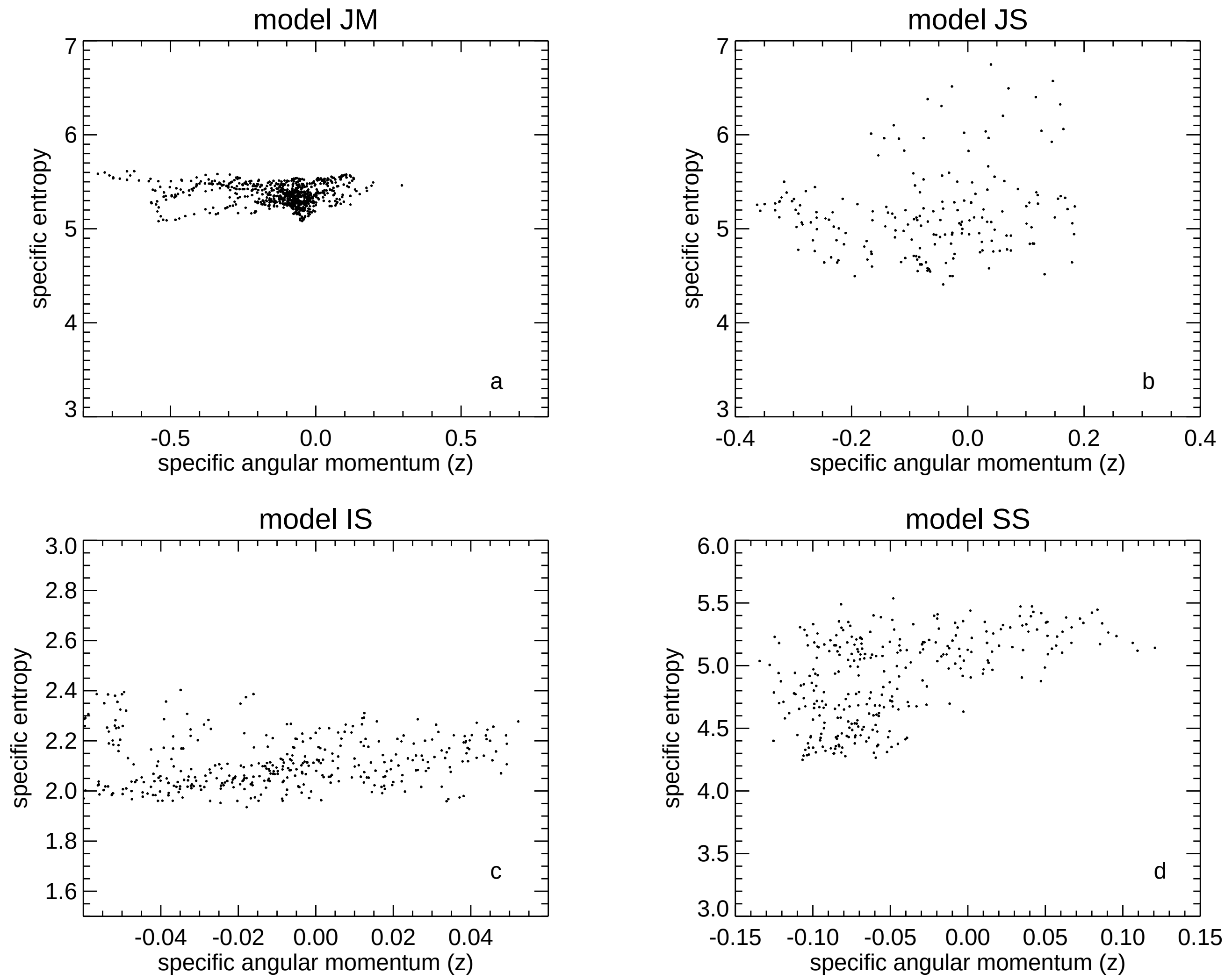

Fig. 16. The specific entropy of accreted matter is plotted versus the specific angular momentum of this matter for models JM, JS, IS and SS. Each dot displays the two quantities at one moment in time. The times for which the dots are plotted are $t \gtrsim 1$, $t! \gtrsim 2$, $t \gtrsim 6$, and $t \gtrsim 3$, respectively.

one accretion radius), radius of the accretor (0.02, 0.1 and 1 accretion radius), and adiabatic index (5/3 and 4/3). The results are compared among the models with differing parameters, to some previously published simulations, and also to the analytic estimates of the specific angular momentum of the matter that is accreted (Eq. (7), which assumes that all angular momentum in the accretion cylinder is actually accreted).

1. All models with a small enough accretor (with a size less or equal than 0.1 accretion radii) exhibit active unstable phases, very similar to the models without gradients. The accretion rates of mass, linear and angular momentum fluctuate with time, although not as strongly as published previously for 2D models (e.g. Fryxell & Taam 1988). Similarly to the 2D simulations, transient disks form around the accretor that alternate their direction of rotation with time.
2. Depending on the model parameters, the average specific angular momentum accreted is roughly between 7% and 70% of the analytical estimate. For the models with small velocity gradients (3%) the accreted specific angular momentum is roughly a factor of 10 smaller than the value of a vortex with Kepler velocity around the surface of the accretor. This factor is roughly 3 for models with a large gradient of 20%.
3. The mass accretion rates of all models with velocity gradients are equal, to within the fluctuation amplitudes, to the rates of the models without gradients (published previously).
4. The fluctuations of the mass accretion rate in the models with small gradients (3%) are also similar to the values of the models without gradients, while the models with large gradients (20%) exhibit larger fluctuations.

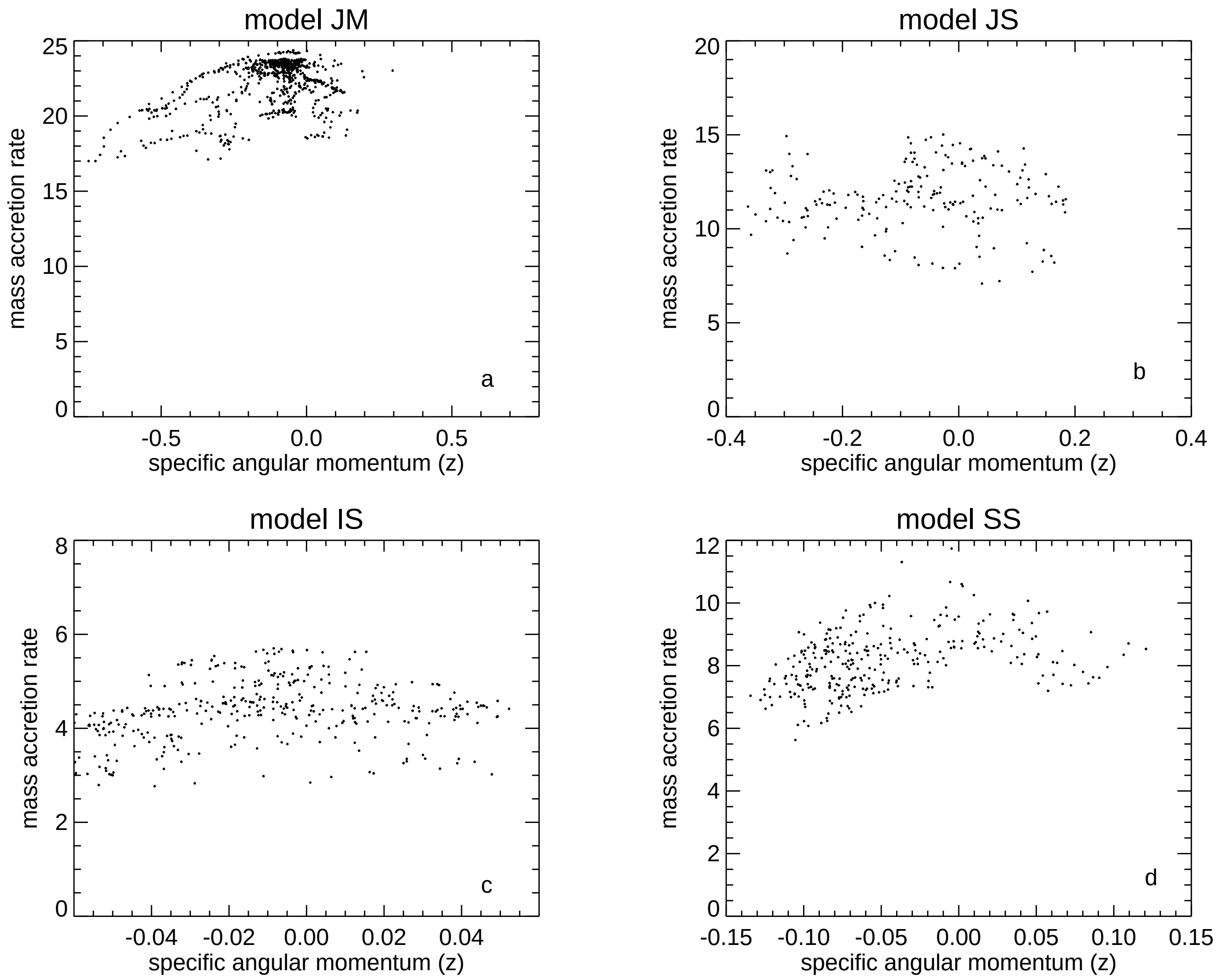

Fig. 17. The mass accretion rate is plotted versus the specific angular momentum of the accreted matter for models JM, JS, IS and SS. Each dot displays the two quantities at one moment in time. The times for which the dots are plotted are $t \gtrsim 1$, $t \gtrsim 2$, $t \gtrsim 6$, and $t \gtrsim 3$, respectively.

So large gradients either amplify existing instability mechanisms or generate new ones.

5. Marginal correlations are found, connecting the mass accretion rate, the specific angular momentum, and the specific entropy during the temporal evolution. The mass accretion rate is maximal when the specific angular momentum is zero, while the specific entropy tends to be smaller when the disks are prograde (i.e. when the specific angular momentum is negative, in our units).

Movies in mpeg format of the dynamical evolution of some models are available in the WWW at `http://www.mpa-garching.mpg.de/~mor/bhla.html`

Acknowledgements. I would like to thank Dr. F. Meyer, Dr. U. Anzer, Dr. T. Foglizzo, and K. Schenker for carefullay reading and correcting the the manuscript and suggesting improvements. The calculations were done at the Rechenzentrum Garching.

References

Anzer U., Börner G., Monaghan J.J., 1987, A&A 176, 235
Anzer U., Börner G., 1995, A&A 299, 62
Balsara D., Livio M., O'Dea C.P., 1994, ApJ 437, 83
Berger M.J., Colella P., 1989, JCP 82, 64
Binney J., Tremaine S., 1987, "Galactic Dynamics", Princeton University Press, New Jersey
Boffin H.M.J., 1991, IAU Symp. 151.
Bondi H., 1952, MNRAS 112, 195
Bondi H., Hoyle F., 1944, MNRAS 104, 273
Chevalier R.A., 1996, ApJ 459, 322
Colella P., Woodward P.R., 1984, JCP 54, 174
Davies R.E., Pringle J., 1980, MNRAS 191, 599
Dodd K.N., McCrea W.H., 1952, MNRAS 112, 205

Drazin P.G., Reid W.H., 1981, in *Hydrodynamic Stability*, Cambridge University Press, Cambridge
Fryxell, B.A., Taam, R.E., 1988, ApJ, 335, 862.
Ho C., Taam R.E., Fryxell B.A., Matsuda T., Koide H., Shima E., 1989, MNRAS 238, 1447
Hoyle F., Lyttleton R.A., 1939, *Proc. Cam. Phil. Soc.* 35, 405
Hoyle F., Lyttleton R.A., 1940a, *Proc. Cam. Phil. Soc.* 36, 323
Hoyle F., Lyttleton R.A., 1940b, *Proc. Cam. Phil. Soc.* 36, 325
Hoyle F., Lyttleton R.A., 1940c, *Proc. Cam. Phil. Soc.* 36, 424
Illarionov A.F., Sunyaev R.A., 1975, A&A 39, 185
Ishii T., Matsuda T., Shima E., Livio M., Anzer U., Börner G., 1993, ApJ 404, 706
Livio M., Soker N., deKool M., Savonije G.J., 1986, MNRAS 222, 235
Mirabel I.F., Paul J., Cordier B., Morris M., Wink J., 1991, A&A 251, L43
Ruffert M., 1994, A&AS 106, 505
Ruffert M., 1995, A&AS 113, 133
Ruffert M., 1996, A&A, in press
Ruffert M., Arnett D., 1994, ApJ 427, 351
Ruffert M., Anzer U., 1995, A&A 295, 108
Ruffert M., Melia F., 1994, A&A 288, L29
Sawada K., Matsuda T., Anzer U., Börner G., Livio M., 1989, A&A 221, 263.
Shapiro S.L., Lightman A.P., 1976, ApJ 204, 555
Taam R.E., Fryxell B.A., 1989, ApJ 339, 297
Wang Y.-M., 1981, A&A 102, 36

This article was processed by the author using Springer-Verlag LaTeX A&A style file *L-AA* version 3.